Journal of Computational Physics 361 (2018) 353–376

Contents lists available at ScienceDirect

Journal of Computational Physics

www.elsevier.com/locate/jcp

Self-consistent adjoint analysis for topology optimization of electromagnetic waves

Yongbo Deng [a,b,*,1], Jan G. Korvink [b,*]

[a] State Key Laboratory of Applied Optics, Changchun Institute of Optics, Fine Mechanics and Physics (CIOMP), Chinese Academy of Sciences, Changchun 130033, China
[b] Institute of Microstructure Technology (IMT), Karlsruhe Institute of Technology (KIT), Hermann-von-Helmholtzplatz 1, Eggenstein-Leopoldshafen 76344, Germany

ARTICLE INFO

Article history:
Received 23 June 2017
Received in revised form 18 December 2017
Accepted 25 January 2018
Available online 2 February 2018

Keywords:
Topology optimization
Self-consistent adjoint sensitivity
Electromagnetic wave
Perfectly matched layers

ABSTRACT

In topology optimization of electromagnetic waves, the Gâteaux differentiability of the conjugate operator to the complex field variable results in the complexity of the adjoint sensitivity, which evolves the original real-valued design variable to be complex during the iterative solution procedure. Therefore, the self-inconsistency of the adjoint sensitivity is presented. To enforce the self-consistency, the real part operator has been used to extract the real part of the sensitivity to keep the real-value property of the design variable. However, this enforced self-consistency can cause the problem that the derived structural topology has unreasonable dependence on the phase of the incident wave. To solve this problem, this article focuses on the self-consistent adjoint analysis of the topology optimization problems for electromagnetic waves. This self-consistent adjoint analysis is implemented by splitting the complex variables of the wave equations into the corresponding real parts and imaginary parts, sequentially substituting the split complex variables into the wave equations with deriving the coupled equations equivalent to the original wave equations, where the infinite free space is truncated by the perfectly matched layers. Then, the topology optimization problems of electromagnetic waves are transformed into the forms defined on real functional spaces instead of complex functional spaces; the adjoint analysis of the topology optimization problems is implemented on real functional spaces with removing the variational of the conjugate operator; the self-consistent adjoint sensitivity is derived, and the phase-dependence problem is avoided for the derived structural topology. Several numerical examples are implemented to demonstrate the robustness of the derived self-consistent adjoint analysis.

© 2018 Elsevier Inc. All rights reserved.

1. Introduction

Control of electromagnetic or optical waves is realized by the structures with complicated geometrical configurations and pre-selected materials. For the complication of electromagnetics, physical intuition-based electromagnetic structure design has its limitations to achieve the desired performance. To overcome these bounds, several inverse design tests have been implemented based on the structural optimization methods [1–21], in which topology optimization method is the most employed one.

* Corresponding authors.
E-mail addresses: dengyb@ciomp.ac.cn (Y. Deng), jan.korvink@kit.edu (J.G. Korvink).
[1] Y. Deng devotes this article to his son J. Deng's four-year-old birthday.

https://doi.org/10.1016/j.jcp.2018.01.045
0021-9991/© 2018 Elsevier Inc. All rights reserved.

Topology optimization is currently regarded to be the most robust methodology for the inverse determination of material distribution in the structures that meet given structural performance criteria. The optimal topology of structures was investigated in 1904 for trusses by Michell and this resulted in the well known Michell type structures [22]. It was developed for elasticity by Bendsøe and Kikuchi [23], and then was extended to a variety of application areas including acoustics, electromagnetics, fluid dynamics and thermodynamics [4–19,24–34], to list the most prominent. Reports on topology optimization in electromagnetics include the applications in beamsplitters [1,2], photonic crystals [3,4], cloaks [5–7], sensors and resonators [33,34], metamaterials [8,9], excitation of surface plasmons [11], and electromagnetic and optical antennas [12,13, 17,20], to list the most prominent. Most of these previous researches on topology optimization of electromagnetic structures are implemented in frequency domain, because the corresponding formulations have better control of the frequency parameters and better resolution for resonance effects. Meanwhile, topology optimization in frequency domain requires fine discretization, and so far scalable parallel iterative solvers do not exist for such type of problems; and large scale problems have been demonstrated in the time domain [35], which has the merit on considering the complex multi-mode designs operating in a wide frequency range.

In frequency domain, the field variables of the electromagnetics are complex, comprising the amplitude and phase of the field. And the cost functions of topology optimization problems are usually include the conjugate of the field variables, e.g. the energy functionals, which are the product of the field variables and their conjugates. The energy functionals are popularly used, because of the well-posedness of their least square forms. For the sensitivity analysis of topology optimization problem, adjoint method is widely used, where the first-order variational is implemented for the corresponding augmented Lagrangian [11]. During the adjoint analysis procedure, it is necessary to implement the variational of the conjugate operation to the field variables. Mathematically, the conjugate operator is Gâteaux differential instead of Fréchet differential, to the field variables [36]. This was ignored in several previous researches, such as the literatures [16,21]. The Gâteaux differentiability of the conjugate operator can cause the incompleteness of the adjoint sensitivity, i.e. the adjoint sensitivity of the real-valued cost functions is complex instead of real for the design variable, which is real-valued distribution defined on the computational domain. If this incomplete sensitivity is used directly, the design variable will be evolved to be complex during the iterative procedure, where the initial of the design variable is set to be real. Then, this adjoint sensitivity is self-inconsistent from the pointview of keeping the real-value property of the design variable. Therefore, the real part extraction operator is used to extract the real part of the derived adjoint sensitivity in [36,37], and to artificially enforce the self-consistency of the adjoint sensitivity. The consequence of such enforced self-inconsistency is that the derived structural topology has dependence on the phase of the incident wave. This phase-dependence is unreasonable, because the incident waves can not be inherently distinguished by only altering their phases.

To solve the problem on the self-inconsistency of the adjoint sensitivity, Fréchet differentiability should be ensured for the cost function. The conjugate operator in the cost function can be removed by splitting the complex field variables into the corresponding real and imaginary parts respectively defined on real functional spaces instead of complex ones, then the Gâteaux differentiability induced by the conjugate operator is avoided. The splitting of the complex variables brings about the splitting of the wave equations, which are complex partial differential equations. The method of splitting complex partial differential equations or variational problems into their corresponding coupled systems for the real and imaginary parts of the field variables has been systematically discussed in [38,39]. Therefore, this article splits the complex variables of the electromagnetic wave equations into the corresponding real parts and imaginary parts, and further derives the coupled equations respectively for the real parts and imaginary parts of the field variables; then the topology optimization problems are transformed into the forms defined on real functional spaces; hence, the adjoint analysis is implemented without implementing the variational of the conjugate operator; furthermore, the self-consistent adjoint sensitivity can be derived, and the phase-dependence problem can be solved for the structural topology. In the adjoint analysis, the derived adjoint equations for the adjoint of the split field variables can be recombined and transformed with deriving the adjoint equations for the adjoint of the original field variables. Therefore, the field variables and their adjoint are solved in complex forms instead of the splitting forms, and this avoids the increase of the complication of the adjoint equations by reducing the field-variable number.

In the following, the density approach is utilized to implement the topology optimization procedure, where the structural topology is determined by the design variable representing the material distribution in the structures [31]. This article is organized as: the topology optimization problems for both the two-dimensional (2D) and three-dimensional (3D) electromagnetic waves are presented in Section 2; in Section 3, the transformation and self-consistent adjoint analysis of the topology optimization problems are implemented by splitting the wave equations with complex variables into the coupled equations with real variables respectively corresponding to the real parts and imaginary parts of the field variables; in Section 4, several numerical examples are provided for both the 2D and 3D cases to demonstrate the performance of the derived self-consistent adjoint sensitivity; the article is concluded and acknowledged in Section 5 and Acknowledgments; and the appendix for relevant mathematical details are supplied in Appendix A. All the mathematical descriptions are performed in the Cartesian coordinate system.

2. Topology optimization problems

Electromagnetic wave propagation is described by the Maxwell's equations. In frequency domain, the Maxwell's equations can be reduced into the wave equations. In order to reduce the dispersion error, the scattered-field formulation of the wave

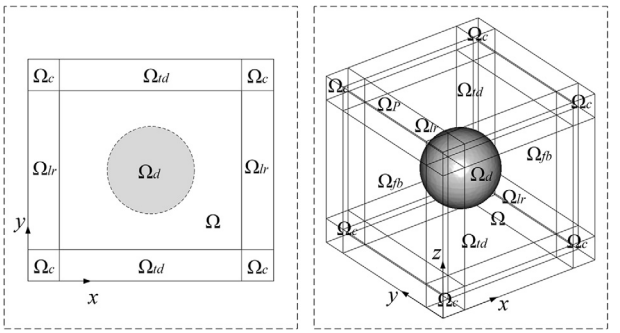

Fig. 1. Sketch for the wave propagating domains and PMLs, where (a) and (b) are respectively for the 2D and 3D problems. The wave propagating domain Ω is enclosed by the PMLs. In the 2D case, the PMLs attached to the sides of Ω are Ω_{lr} and Ω_{td}, respectively perpendicular to x-axis and y-axis; the PML domains at the vertexes are Ω_c. In the 3D case, the PMLs attached to the surfaces of Ω are Ω_{fb}, Ω_{lr} and Ω_{td}, respectively perpendicular to x-axis, y-axis and z-axis; the PMLs attached to the edges along x-axis, y-axis and z-axis are Ω_{fbe}, Ω_{lre} and Ω_{tde}; the PML domains at the vertexes are Ω_c. For both cases, the design domain Ω_d is a subdomain of the wave propagating domain Ω; the union of all PMLs is marked to be Ω_P; the union of the external boundaries is $\Gamma_D = \partial(\Omega \cup \Omega_P)$.

equations are used with time harmonic factor $e^{j\omega t}$, where $j = \sqrt{-1}$ is the imaginary unit, ω is the angular frequency and t is the time.

For the waves that can be reduced into 2D, the transverse magnetic (TM) waves with polarization perpendicular to the wave plane are the more general cases. This is because that the TM waves can both include the description of related physics with dielectrics and noble metal, where the surface plasmonics can not be presented in the transverse electric (TE) waves [41]. Therefore, this article focuses on the TM waves for the 2D cases. Without losing the generality, it can also be extended to the transverse electric (TE) waves with the similar procedure. For the TM wave, the wave equation is

$$\nabla \cdot \left[\epsilon_r^{-1} \nabla (H_{sz} + H_{iz})\right] + k_0^2 \mu_r (H_{sz} + H_{iz}) = 0, \text{ in } \Omega \tag{1}$$

where the TM wave is polarized in the z-direction; ∇ is the gradient operator in the Cartesian coordinate system; $H_z = H_{sz} + H_{iz}$ is the total field, H_{sz} and H_{iz} are the scattering and incident fields, respectively; ϵ_r and μ_r are the relative permittivity and permeability, respectively; $k_0 = \omega\sqrt{\epsilon_0 \mu_0}$ is the free space wave number with ϵ_0 and μ_0 respectively representing the free space permittivity and permeability; Ω is a square-shaped wave propagating domain.

For the waves that can not be reduced into 2D (e.g. electromagnetic waves scattered by the objects with complicated geometrical configurations), the 3D wave equation is used to describe the wave propagation

$$\begin{aligned} &\nabla \times \left[\mu_r^{-1} \nabla \times (\mathbf{E}_s + \mathbf{E}_i)\right] - k_0^2 \epsilon_r (\mathbf{E}_s + \mathbf{E}_i) = \mathbf{0}, \text{ in } \Omega \\ &\nabla \cdot [\epsilon_r (\mathbf{E}_s + \mathbf{E}_i)] = 0, \text{ in } \Omega \end{aligned} \tag{2}$$

where the electric field $\mathbf{E} = \mathbf{E}_s + \mathbf{E}_i$ is the total field, $\mathbf{E}_s$ and $\mathbf{E}_i$ are respectively the scattering and incident fields; the second equation is the divergence-free condition of the electric displacement; Ω is a cuboid-shaped wave propagating domain.

The incident waves in equations (1) and (2) are the electromagnetic waves propagating in the background of the computational domain. The infinite computational space is truncated by the perfectly matched layers (PMLs), which are implemented by solving the wave equations with the complex-valued coordinate transformation [40,42,43]: for the 2D cases,

$$\nabla_{\mathbf{x}'} \cdot \left(\epsilon_r^{-1} \nabla_{\mathbf{x}'} H_{sz}\right) + k_0^2 \mu_r H_{sz} = 0, \text{ in } \Omega_P \tag{3}$$

for the 3D cases,

$$\begin{aligned} &\nabla_{\mathbf{x}'} \times \left(\mu_r^{-1} \nabla_{\mathbf{x}'} \times \mathbf{E}_s\right) - k_0^2 \epsilon_r \mathbf{E}_s = \mathbf{0}, \text{ in } \Omega_P \\ &\nabla \cdot \mathbf{E}_s = 0, \text{ in } \Omega_P \end{aligned} \tag{4}$$

where $\mathbf{x}'$ is the complex-valued coordinate transformed from the original Cartesian coordinate in Ω_P; $\mathbf{E}_s$ in the PMLs satisfies the divergence-free condition described in the original Cartesian coordinate system, because the fields are source-free in the PMLs; $\nabla_{\mathbf{x}'}$ is the gradient operator in the PMLs with transformed coordinates; Ω_P is the union of the PML domains Ω_{fb}, Ω_{lr}, Ω_{td}, Ω_{fbe}, Ω_{lre}, Ω_{tde} and Ω_c, sketched in Fig. 1. The transformed coordinates and the original Cartesian coordinates satisfy the transformation

$$\mathbf{x}' = \mathbf{T}\mathbf{x}, \ \forall \mathbf{x} \in \Omega_P \tag{5}$$

with $\mathbf{T}$ and $\mathbf{x}$ respectively representing the transformation matrix and the original Cartesian coordinate. For the 2D cases, the transformation matrix is [40]

$$\mathbf{T}=\begin{cases}\begin{pmatrix}(1-j)\,\lambda/d & 0\\ 0 & 1\end{pmatrix},\ \text{in } \Omega_{lr}\\ \begin{pmatrix}1 & 0\\ 0 & (1-j)\,\lambda/d\end{pmatrix},\ \text{in } \Omega_{td}\\ \begin{pmatrix}(1-j)\,\lambda/d & 0\\ 0 & (1-j)\,\lambda/d\end{pmatrix},\ \text{in } \Omega_{c}\end{cases} \tag{6}$$

for the 3D cases, the transformation matrix is [40]

$$\mathbf{T}=\begin{cases}\begin{pmatrix}(1-j)\,\lambda/d & 0 & 0\\ 0 & 1 & 0\\ 0 & 0 & 1\end{pmatrix},\ \text{in } \Omega_{fb}\\ \begin{pmatrix}1 & 0 & 0\\ 0 & (1-j)\,\lambda/d & 0\\ 0 & 0 & 1\end{pmatrix},\ \text{in } \Omega_{lr}\\ \begin{pmatrix}1 & 0 & 0\\ 0 & 1 & 0\\ 0 & 0 & (1-j)\,\lambda/d\end{pmatrix},\ \text{in } \Omega_{td}\\ \begin{pmatrix}1 & 0 & 0\\ 0 & (1-j)\,\lambda/d & 0\\ 0 & 0 & (1-j)\,\lambda/d\end{pmatrix},\ \text{in } \Omega_{fbe}\\ \begin{pmatrix}(1-j)\,\lambda/d & 0 & 0\\ 0 & 1 & 0\\ 0 & 0 & (1-j)\,\lambda/d\end{pmatrix},\ \text{in } \Omega_{lre}\\ \begin{pmatrix}(1-j)\,\lambda/d & 0 & 0\\ 0 & (1-j)\,\lambda/d & 0\\ 0 & 0 & 1\end{pmatrix},\ \text{in } \Omega_{tde}\\ \begin{pmatrix}(1-j)\,\lambda/d & 0 & 0\\ 0 & (1-j)\,\lambda/d & 0\\ 0 & 0 & (1-j)\,\lambda/d\end{pmatrix},\ \text{in } \Omega_{c}\end{cases} \tag{7}$$

where λ the incident wavelength in the truncated background, and d the thickness of the PMLs. The no-jump boundary condition for the scattering field is imposed on the interface $\partial\Omega$ between Ω_P and Ω

$$\begin{aligned}&\epsilon_r^{-1}\left(\nabla H_{sz}-\nabla_{\mathbf{x}'}H_{sz}\right)\cdot\mathbf{n}=0,\ \text{on } \partial\Omega\\ \text{or }&\mu_r^{-1}\left(\nabla\times\mathbf{E}_s-\nabla_{\mathbf{x}'}\times\mathbf{E}_s\right)\times\mathbf{n}=\mathbf{0},\ \text{on } \partial\Omega\end{aligned} \tag{8}$$

where $\mathbf{n}$ is the outward unitary normal. The perfect magnetic ($H_{sz}=0$) and electric conductor ($\mathbf{n}\times\mathbf{E}_s=\mathbf{0}$) conditions are imposed on the external boundaries $\Gamma_D=\partial\left(\Omega\cup\Omega_P\right)$ of the PMLs respectively for the 2D and 3D cases.

The density approach for topology optimization is based on the material interpolation between two different materials, where the material interpolation is implemented by the binarily valued design variable [31]. The considered materials are nonmagnetic. Therefore, the design variable is introduced as a relative material density to interpolate two different permittivities. To ensure the robust evolution, the continuous design variable is sequentially filtered, elementwised and projected; then the projected design variable, named physical density, takes the place of the design variable to implement the material interpolation [44]. The design variable is filtered by solving the following PDE filter equation [45]

$$\begin{aligned}&-r^2\nabla\cdot\nabla\gamma_f+\gamma_f=\gamma,\ \text{in } \Omega_d\subset\Omega\\ &\mathbf{n}\cdot\nabla\gamma_f=0,\ \text{in } \partial\Omega_d\end{aligned} \tag{9}$$

where r is the filtering radius; γ is the design variable; γ_f is the filtered design variable; Ω_d is the design domain. The elementwise operation, with deriving the elementwise design variable γ_e, is carried out by averaging the filtered design variable on every piece of the design domain, which is divided into disjoint pieces to ensure the piecewise homogeneity of the materials in the design domain [15]:

$$\gamma_e = \sum_{n=1}^{N} \frac{1}{V_n} \int_{P_n} \gamma_f \, \mathrm{d}\Omega, \text{ with } V_n = \int_{P_n} 1 \, \mathrm{d}\Omega, \ \bigcup_{n=1}^{N} P_n = \Omega_d, \ P_l \bigcap P_m = \emptyset \ (l, m = 1, 2 \cdots N, \ l \neq m) \tag{10}$$

This elementwise operation decouples the design variable with the divergence-free condition with reducing the divergence-free condition of equation (2) to be $\nabla \cdot \mathbf{E}_s = 0$; then the wave equation (2) can be solved using the edge element-based finite element method with Nedelec elements to avoid the spurious solutions [47,48]. The projection of the elementwise design variable is implemented by the threshold method [51,52]

$$\gamma_p = \frac{\tanh(\beta\xi) + \tanh(\beta(\gamma_e - \xi))}{\tanh(\beta\xi) + \tanh(\beta(1 - \xi))} \tag{11}$$

where $\xi \in [0, 1]$ and β are the threshold and projection parameters, respectively; for the choice of the values of ξ and β, one can refer to [51,52].

In topology optimization for electromagnetic waves, two material interpolation formulations are usually utilized. The first one is the linear formulation [5,6]

$$\epsilon_r(\gamma_p) = \epsilon_{rl} + \gamma_p(\epsilon_{rh} - \epsilon_{rl}), \text{ in } \Omega_d \tag{12}$$

where ϵ_{rl} and ϵ_{rh} are the two relative permittivities. This linear formulation is more suitable for two dielectric materials with relatively low contrast between the relative permittivities. The second formulation is the hybrid of logarithmic and power law approaches [8,53]

$$\epsilon_r(\gamma_p) = 10^{\log\epsilon_{rh} - \frac{1-\gamma_p^3}{1+\gamma_p^3}(\log\epsilon_{rh} - \log\epsilon_{rl})}, \text{ in } \Omega_d \tag{13}$$

and this hybrid formulation is more suitable for two materials with relatively high contrast between the relative permittivities. The surface plasmons is one typical case with two high-contrast materials (noble metal and dielectrics), where the electromagnetic field decays exponentially. The destination of the hybrid formulation is to mimic the exponential decaying of the electromagnetic field at the metal–dielectric interface.

With the generally formed cost function defined on the computational domain, the topology optimization problems can be constructed as follows: for the 2D cases

$$\begin{aligned} \text{min or max } & J = \int_{\Omega} A\left(H_{sz}, H_{sz}^*, \nabla H_{sz}, \nabla H_{sz}^*, \gamma_p; \gamma\right) \mathrm{d}\Omega \\ \text{s.t. } & \nabla \cdot \left[\epsilon_r^{-1} \nabla (H_{sz} + H_{iz})\right] + k_0^2 \mu_r (H_{sz} + H_{iz}) = 0, \text{ in } \Omega \\ & \nabla_{\mathbf{x}'} \cdot \left(\epsilon_r^{-1} \nabla_{\mathbf{x}'} H_{sz}\right) + k_0^2 \mu_r H_{sz} = 0, \text{ in } \Omega_P \\ & -r^2 \nabla \cdot \nabla \gamma_f + \gamma_f = \gamma, \text{ in } \Omega_d \end{aligned} \tag{14}$$

for the 3D cases

$$\begin{aligned} \text{min or max } & J = \int_{\Omega} A\left(\mathbf{E}_s, \mathbf{E}_s^*, \nabla \times \mathbf{E}_s, \nabla \times \mathbf{E}_s^*, \gamma_p; \gamma\right) \mathrm{d}\Omega \\ \text{s.t. } & \nabla \times \left[\mu_r^{-1} \nabla \times (\mathbf{E}_s + \mathbf{E}_i)\right] - k_0^2 \epsilon_r (\mathbf{E}_s + \mathbf{E}_i) = \mathbf{0}, \text{ in } \Omega \\ & \nabla_{\mathbf{x}'} \times \left(\mu_r^{-1} \nabla_{\mathbf{x}'} \times \mathbf{E}_s\right) - k_0^2 \epsilon_r \mathbf{E}_s = \mathbf{0}, \text{ in } \Omega_P \\ & \nabla \cdot \mathbf{E}_s = 0, \text{ in } \Omega \cup \Omega_P \\ & -r^2 \nabla \cdot \nabla \gamma_f + \gamma_f = \gamma, \text{ in } \Omega_d \end{aligned} \tag{15}$$

where A is the integral functional of the field variables; $*$ is the conjugate operation of a complex.

3. Transformation and adjoint analysis

The iterative procedure is the usual approach to solve the topology optimization problems in equations (14) and (15). In the iterative approach, the design variable is evolved based on the gradient information of the cost function. The gradient information can be efficiently derived by the adjoint method [54], which is implemented based on the first order variational of the augmented Lagrangian of the optimization problems in equations (14) and (15). However, the integral functional A of the cost function contains the conjugate of the field variables, which is Gâteaux differential instead of Fréchet differential. This results in the complexity of the adjoint sensitivity, which is self-inconsistent. The self-inconsistency of the sensitivity further results in that the derived structural topology has dependence on the phase of the incident wave. And the effect of the self-inconsistent adjoint sensitivity will be demonstrated by the numerical examples in Section 4.1.

To solve the problem on self-inconsistency of the adjoint sensitivity, the wave equations in equations (1) and (2) can be transformed by splitting the complex variables into the real parts and imaginary parts. By setting $H_{sz} = H_{sz}^R + jH_{sz}^I$, $H_{iz} = H_{iz}^R + jH_{iz}^I$, $\epsilon_r^{-1} = \left(\epsilon_r^{-1}\right)^R + j\left(\epsilon_r^{-1}\right)^I$, and substituting these split variables into equation (1), the 2D wave equation is transformed into

$$\begin{aligned}
&\nabla\cdot\left[\left(\epsilon_r^{-1}\right)^R\nabla\left(H_{sz}^R+H_{iz}^R\right)-\left(\epsilon_r^{-1}\right)^I\nabla\left(H_{sz}^I+H_{iz}^I\right)\right]+k_0^2\mu_r\left(H_{sz}^R+H_{iz}^R\right)=0,\ \text{in }\Omega\\
&\nabla\cdot\left[\left(\epsilon_r^{-1}\right)^I\nabla\left(H_{sz}^R+H_{iz}^R\right)+\left(\epsilon_r^{-1}\right)^R\nabla\left(H_{sz}^I+H_{iz}^I\right)\right]+k_0^2\mu_r\left(H_{sz}^I+H_{iz}^I\right)=0,\ \text{in }\Omega
\end{aligned}\tag{16}$$

where the superscripts R and I are respectively used to mark the real part and imaginary part of the corresponding complex variable; the scattering boundary conditions for H_{sz}^R and H_{sz}^I are respectively implemented by solving the split wave equation in the PMLs with complex-valued coordinate transformation and zero-incident field

$$\begin{aligned}
&\nabla_{\mathbf{x}'}\cdot\left[\left(\epsilon_r^{-1}\right)^R\nabla_{\mathbf{x}'}H_{sz}^R-\left(\epsilon_r^{-1}\right)^I\nabla_{\mathbf{x}'}H_{sz}^I\right]+k_0^2\mu_r\left(H_{sz}^R+H_{iz}^R\right)=0,\ \text{in }\Omega_P\\
&\nabla_{\mathbf{x}'}\cdot\left[\left(\epsilon_r^{-1}\right)^I\nabla_{\mathbf{x}'}H_{sz}^R+\left(\epsilon_r^{-1}\right)^R\nabla_{\mathbf{x}'}H_{sz}^I\right]+k_0^2\mu_r\left(H_{sz}^I+H_{iz}^I\right)=0,\ \text{in }\Omega_P
\end{aligned}\tag{17}$$

Similarly, by setting $\mathbf{E}_s = \mathbf{E}_s^R + j\mathbf{E}_s^I$, $\mathbf{E}_i = \mathbf{E}_i^R + j\mathbf{E}_i^I$, $\epsilon_r = \epsilon_r^R + j\epsilon_r^I$, and substituting these split variables into equation (2), the 3D wave equation is transformed into

$$\begin{aligned}
&\nabla\times\left[\mu_r^{-1}\nabla\times\left(\mathbf{E}_s^R+\mathbf{E}_i^R\right)\right]-k_0^2\left[\epsilon_r^R\left(\mathbf{E}_s^R+\mathbf{E}_i^R\right)-\epsilon_r^I\left(\mathbf{E}_s^I+\mathbf{E}_i^I\right)\right]=\mathbf{0},\ \text{in }\Omega\\
&\nabla\cdot\mathbf{E}_s^R=0,\ \text{in }\Omega\\
&\nabla\times\left[\mu_r^{-1}\nabla\times\left(\mathbf{E}_s^I+\mathbf{E}_i^I\right)\right]-k_0^2\left[\epsilon_r^I\left(\mathbf{E}_s^R+\mathbf{E}_i^R\right)+\epsilon_r^R\left(\mathbf{E}_s^I+\mathbf{E}_i^I\right)\right]=\mathbf{0},\ \text{in }\Omega\\
&\nabla\cdot\mathbf{E}_s^I=0,\ \text{in }\Omega
\end{aligned}\tag{18}$$

where the scattering boundary conditions for $\mathbf{E}_s^R$ and $\mathbf{E}_s^I$ are respectively implemented by solving

$$\begin{aligned}
&\nabla_{\mathbf{x}'}\times\left(\mu_r^{-1}\nabla_{\mathbf{x}'}\times\mathbf{E}_s^R\right)-k_0^2\left(\epsilon_r^R\mathbf{E}_s^R-\epsilon_r^I\mathbf{E}_s^I\right)=\mathbf{0},\ \text{in }\Omega_P\\
&\nabla\cdot\mathbf{E}_s^R=0,\ \text{in }\Omega_P\\
&\nabla_{\mathbf{x}'}\times\left(\mu_r^{-1}\nabla_{\mathbf{x}'}\times\mathbf{E}_s^I\right)-k_0^2\left(\epsilon_r^I\mathbf{E}_s^R+\epsilon_r^R\mathbf{E}_s^I\right)=\mathbf{0},\ \text{in }\Omega_P\\
&\nabla\cdot\mathbf{E}_s^I=0,\ \text{in }\Omega_P
\end{aligned}\tag{19}$$

And the other boundary conditions for equations (1) and (2) can also be split following the similar procedure. Furthermore, the topology optimization problems in equations (14) and (15) are transformed into

$$\begin{aligned}
\min\text{ or }\max\ J=&\int_\Omega A\left(H_{sz}^R,H_{sz}^I,\nabla H_{sz}^R,\nabla H_{sz}^I,\gamma_p;\gamma\right)\mathrm{d}\Omega\\
\text{s.t. }&\nabla\cdot\left[\left(\epsilon_r^{-1}\right)^R\nabla\left(H_{sz}^R+H_{iz}^R\right)-\left(\epsilon_r^{-1}\right)^I\nabla\left(H_{sz}^I+H_{iz}^I\right)\right]+k_0^2\mu_r\left(H_{sz}^R+H_{iz}^R\right)=0,\ \text{in }\Omega\\
&\nabla\cdot\left[\left(\epsilon_r^{-1}\right)^I\nabla\left(H_{sz}^R+H_{iz}^R\right)+\left(\epsilon_r^{-1}\right)^R\nabla\left(H_{sz}^I+H_{iz}^I\right)\right]+k_0^2\mu_r\left(H_{sz}^I+H_{iz}^I\right)=0,\ \text{in }\Omega\\
&\nabla_{\mathbf{x}'}\cdot\left[\left(\epsilon_r^{-1}\right)^R\nabla_{\mathbf{x}'}H_{sz}^R-\left(\epsilon_r^{-1}\right)^I\nabla_{\mathbf{x}'}H_{sz}^I\right]+k_0^2\mu_r\left(H_{sz}^R+H_{iz}^R\right)=0,\ \text{in }\Omega_P\\
&\nabla_{\mathbf{x}'}\cdot\left[\left(\epsilon_r^{-1}\right)^I\nabla_{\mathbf{x}'}H_{sz}^R+\left(\epsilon_r^{-1}\right)^R\nabla_{\mathbf{x}'}H_{sz}^I\right]+k_0^2\mu_r\left(H_{sz}^I+H_{iz}^I\right)=0,\ \text{in }\Omega_P\\
&-r^2\nabla\cdot\nabla\gamma_f+\gamma_f=\gamma,\ \text{in }\Omega_d
\end{aligned}\tag{20}$$

and

$$
\begin{aligned}
\text{min or max } J = & \int_{\Omega} A\left(\mathbf{E}_s^R, \mathbf{E}_s^I, \nabla\times\mathbf{E}_s^R, \nabla\times\mathbf{E}_s^I, \gamma_p; \gamma\right) \mathrm{d}\Omega \\
\text{s.t. } & \nabla\times\left[\mu_r^{-1}\nabla\times\left(\mathbf{E}_s^R+\mathbf{E}_i^R\right)\right] - k_0^2\left[\epsilon_r^R\left(\mathbf{E}_s^R+\mathbf{E}_i^R\right) - \epsilon_r^I\left(\mathbf{E}_s^I+\mathbf{E}_i^I\right)\right] = \mathbf{0},\ \text{in } \Omega \\
& \nabla\times\left[\mu_r^{-1}\nabla\times\left(\mathbf{E}_s^I+\mathbf{E}_i^I\right)\right] - k_0^2\left[\epsilon_r^I\left(\mathbf{E}_s^R+\mathbf{E}_i^R\right) + \epsilon_r^R\left(\mathbf{E}_s^I+\mathbf{E}_i^I\right)\right] = \mathbf{0},\ \text{in } \Omega \\
& \nabla_{\mathbf{x}'}\times\left(\mu_r^{-1}\nabla_{\mathbf{x}'}\times\mathbf{E}_s^R\right) - k_0^2\left(\epsilon_r^R\mathbf{E}_s^R - \epsilon_r^I\mathbf{E}_s^I\right) = \mathbf{0},\ \text{in } \Omega_P \\
& \nabla_{\mathbf{x}'}\times\left(\mu_r^{-1}\nabla_{\mathbf{x}'}\times\mathbf{E}_s^I\right) - k_0^2\left(\epsilon_r^I\mathbf{E}_s^R + \epsilon_r^R\mathbf{E}_s^I\right) = \mathbf{0},\ \text{in } \Omega_P \\
& \nabla\cdot\mathbf{E}_s^R = 0,\ \text{in } \Omega\cup\Omega_P \\
& \nabla\cdot\mathbf{E}_s^I = 0,\ \text{in } \Omega\cup\Omega_P \\
& -r^2\nabla\cdot\nabla\gamma_f + \gamma_f = \gamma,\ \text{in } \Omega_d
\end{aligned}
\tag{21}
$$

Because the real parts and imaginary parts of the field variables are valued in real functional spaces, the conjugate operation is removed from the transformed topology optimization problems. Then, the Fréchet differentiability, on the reasonably chosen functional spaces of the real variables, is ensured in the first order variational analysis of the augmented Lagrangian corresponding to equations (20) and (21).

Based on the Lagrangian multiplier-based adjoint method and the adjoint analysis of the transformed topology optimization problem in equation (20), the weak forms of the adjoint equations for the topology optimization problem in equation (14) are derived to be (the details are presented in Appendix A.1): find $\hat{H}_{sz}$ with $Re\left(\hat{H}_{sz}\right)\in\mathcal{H}\left(\Omega\cup\Omega_P\right)$, $Im\left(\hat{H}_{sz}\right)\in\mathcal{H}\left(\Omega\cup\Omega_P\right)$ and $\hat{H}_{sz}=0$ on Γ_D, satisfying

$$
\begin{aligned}
&\int_{\Omega}\left(\frac{\partial A}{\partial Re\left(H_{sz}\right)} - j\frac{\partial A}{\partial Im\left(H_{sz}\right)}\right)\phi + \left(\frac{\partial A}{\partial\nabla Re\left(H_{sz}\right)} - j\frac{\partial A}{\partial\nabla Im\left(H_{sz}\right)}\right)\cdot\nabla\phi - \epsilon_r^{-1}\nabla\hat{H}_{sz}^*\cdot\nabla\phi \\
&+ k_0^2\mu_r\hat{H}_{sz}^*\phi\,\mathrm{d}\Omega + \int_{\Omega_P} -\epsilon_r^{-1}\left(\mathbf{T}\nabla\hat{H}_{sz}^*\right)\cdot\left(\mathbf{T}\nabla\phi\right)|\mathbf{T}|^{-1} + k_0^2\mu_r\hat{H}_{sz}^*\phi\,|\mathbf{T}|\,\mathrm{d}\Omega = 0,\ \forall\phi\in\mathcal{H}\left(\Omega\cup\Omega_P\right)\ \text{(for the 2D case)}
\end{aligned}
\tag{22}
$$

find $\hat{\gamma}_f\in\mathcal{H}\left(\Omega_d\right)$ satisfying

$$
\begin{aligned}
&\int_{\Omega_d} r^2\nabla\hat{\gamma}_f\cdot\nabla\varphi + \hat{\gamma}_f\varphi + \left[\sum_{n=1}^{N}\frac{1}{V_n}\int_{P_n}\frac{\partial A}{\partial\gamma_p}\frac{\partial\gamma_p}{\partial\gamma_e} - Re\left(\frac{\partial\epsilon_r^{-1}}{\partial\gamma_p}\frac{\partial\gamma_p}{\partial\gamma_e}\nabla\left(H_{sz}+H_{iz}\right)\right)\cdot Re\left(\nabla\hat{H}_{sz}^*\right)\right. \\
&\left. + Im\left(\frac{\partial\epsilon_r^{-1}}{\partial\gamma_p}\frac{\partial\gamma_p}{\partial\gamma_e}\nabla\left(H_{sz}+H_{iz}\right)\right)\cdot Im\left(\nabla\hat{H}_{sz}^*\right)\mathrm{d}\Omega\right]\varphi\,\mathrm{d}\Omega = 0,\ \forall\varphi\in\mathcal{H}\left(\Omega_d\right)\ \text{(for the 2D case)}
\end{aligned}
\tag{23}
$$

where $\hat{H}_{sz}$ and $\hat{\gamma}_f$ are the adjoint variables of H_{sz} and γ_f, respectively; * is the operator used to implement the conjugate of a complex variable; Γ_D is the perfect magnetic conductor boundary; $\mathcal{H}\left(\Omega\cup\Omega_P\right)$ and $\mathcal{H}\left(\Omega_d\right)$ are the first order Hilbert spaces for the real functions defined on $\Omega\cup\Omega_P$ and Ω_d, respectively; Re and Im are operators used to extract the real part and imaginary part of a complex. And the adjoint sensitivity is derived to be

$$
\delta\hat{J} = \int_{\Omega_d}\left(\frac{\partial A}{\partial\gamma} - \hat{\gamma}_f\right)\delta\gamma\,\mathrm{d}\Omega,\ \gamma\in\mathcal{L}^2\left(\Omega_d\right)\ \text{(for the 2D case)}
\tag{24}
$$

where $\delta\gamma$ is the first order variational of γ; $\hat{\gamma}_f$ is derived by sequentially solving equations (22) and (23); $\mathcal{L}^2\left(\Omega_d\right)$ is the second order Lebesque space for the real functions defined on Ω_d.

Based on the similar procedure, the weak forms of the adjoint equations for the topology optimization problem in equation (21) can be derived to be (the details are presented in Appendix A.2): find $\hat{\mathbf{E}}_s$ with $Re\left(\hat{\mathbf{E}}_s\right)\in\mathcal{V}_{\mathbf{E}}$, $Im\left(\hat{\mathbf{E}}_s\right)\in\mathcal{V}_{\mathbf{E}}$ and $\mathbf{n}\times\hat{\mathbf{E}}_s=\mathbf{0}$ on Γ_D, satisfying

$$\int_{\Omega}\left(\frac{\partial A}{\partial Re\left(\mathbf{E}_s\right)}-j\frac{\partial A}{\partial Im\left(\mathbf{E}_s\right)}\right)\cdot\boldsymbol{\phi}+\left(\frac{\partial A}{\partial\nabla\times Re\left(\mathbf{E}_s\right)}-j\frac{\partial A}{\partial\nabla\times Im\left(\mathbf{E}_s\right)}\right)\cdot\left(\nabla\times\boldsymbol{\phi}\right)$$
$$+\mu_r^{-1}\left(\nabla\times\hat{\mathbf{E}}_s^*\right)\cdot\left(\nabla\times\boldsymbol{\phi}\right)-k_0^2\epsilon_r\hat{\mathbf{E}}_s^*\cdot\boldsymbol{\phi}\,\mathrm{d}\Omega+\int_{\Omega_P}\mu_r^{-1}\left(\mathbf{T}\nabla\times\hat{\mathbf{E}}_s^*\right)\cdot\left(\mathbf{T}\nabla\times\boldsymbol{\phi}\right)|\mathbf{T}|^{-1} \tag{25}$$
$$-k_0^2\epsilon_r\hat{\mathbf{E}}_s^*\cdot\boldsymbol{\phi}\,|\mathbf{T}|\,\mathrm{d}\Omega=0,\forall\boldsymbol{\phi}\in\mathcal{V}_{\mathbf{E}}\ \text{(for the 3D case)}$$

find $\hat{\gamma}_f\in\mathcal{H}\left(\Omega_d\right)$ satisfying

$$\int_{\Omega_d}r^2\nabla\hat{\gamma}_f\cdot\nabla\varphi+\hat{\gamma}_f\varphi+\left[\sum_{n=1}^{N}\frac{1}{V_n}\int_{P_n}\frac{\partial A}{\partial\gamma_p}\frac{\partial\gamma_p}{\partial\gamma_e}-Re\left(k_0^2\frac{\partial\epsilon_r}{\partial\gamma_p}\frac{\partial\gamma_p}{\partial\gamma_e}\left(\hat{\mathbf{E}}_s+\hat{\mathbf{E}}_i\right)\right)\cdot Re\left(\hat{\mathbf{E}}_s^*\right)\right.$$
$$\left.+Im\left(k_0^2\frac{\partial\epsilon_r}{\partial\gamma_p}\frac{\partial\gamma_p}{\partial\gamma_e}\left(\hat{\mathbf{E}}_s+\hat{\mathbf{E}}_i\right)\right)\cdot Im\left(\hat{\mathbf{E}}_s^*\right)\mathrm{d}\Omega\right]\varphi\,\mathrm{d}\Omega=0,\ \forall\varphi\in\mathcal{H}\left(\Omega_d\right)\ \text{(for the 3D case)} \tag{26}$$

where $\hat{\mathbf{E}}_s$ and $\hat{\gamma}_f$ are the adjoint variables of $\mathbf{E}_s$ and γ_f, respectively; $\mathcal{V}_{\mathbf{E}}\doteq\left\{\mathbf{u}\in\mathcal{H}\left(\mathrm{curl};\Omega\cup\Omega_P\right)\middle|\nabla\cdot\mathbf{u}=0\ \text{in}\ \Omega\cup\Omega_P\right\}$ with $\mathcal{H}\left(\mathrm{curl};\Omega\cup\Omega_P\right)=\left\{\mathbf{u}\in\left(\mathcal{L}^2\left(\Omega\cup\Omega_P\right)\right)^3\middle|\nabla\times\mathbf{u}\in\left(\mathcal{L}^2\left(\Omega\cup\Omega_P\right)\right)^3\right\}$; $\mathcal{L}^2\left(\Omega\cup\Omega_P\right)$ represents the second order Lebesque space for the real functionals defined on $\Omega\cup\Omega_P$. And the adjoint sensitivity is

$$\delta\hat{J}=\int_{\Omega_d}\left(\frac{\partial A}{\partial\gamma}-\hat{\gamma}_f\right)\delta\gamma\,\mathrm{d}\Omega,\ \gamma\in\mathcal{L}^2\left(\Omega_d\right)\ \text{(for the 3D case)} \tag{27}$$

where $\hat{\gamma}_f$ is derived by sequentially solving equations (25) and (26).

After the adjoint analysis, the derived adjoint sensitivity can be used to determine the evolution direction of the design variables in the iterative solution of the topology optimization problems. From equations (23) and (26), one can confirm that the adjoint variable $\hat{\gamma}_f$ is real. In addition, the integral functional A and the design variable are both real. Hence, the adjoint sensitivities in equations (24) and (27) are real. The adjoint analysis is complete, because the Fréchet differentiability is ensured by splitting the field variables of the wave equations into the real parts and imaginary parts. Therefore, the derived adjoint sensitivity is self-consistent.

4. Numerical examples

Numerical examples are presented to demonstrate the topology optimization procedure with the design variable evolved by the introduced self-consistent adjoint sensitivity. These numerical examples include the 2D and 3D dielectric cloaks with real permittivity, and 2D and 3D nanostructures with complex permittivity for localized surface plasmonic resonances (LSPRs).

In the numerical examples, the topology optimization problems are solved by a gradient-based iterative procedure, where the gradient information is derived by the self-consistent adjoint sensitivity. The flowchart for iterative solution of the optimization problems is shown in Fig. 2. The iterative procedure includes the following steps:

1) initialize the design variable and optimization parameters;
2) solve the wave equations with the current design variable and compute the value of the design objective;
3) solve the adjoint equations based on the solution of the wave equations;
4) compute the adjoint derivative of the design objective;
5) update the design variable using the method of moving asymptotes (MMA) [46];
6) do postprocessing, if the stopping criteria are satisfied; or else, return to the second step.

In this solution procedure, the filter radius r of the PDE filter in equation (9) is set to be 2/15 of the incident wavelength; the threshold parameter ξ in equation (11) is set to be 0.5; the initial value of the projection parameter β is set to be 1 and it is doubled after every fixed number of iterations until the preset maximal value 2^{10} is reached. The above steps are implemented iteratively until the stopping criteria are satisfied, and the stopping criteria are specified to be the maximal iteration number and the change of the objective values in five consecutive iterations satisfying

$$\frac{1}{5}\sum_{i=1}^{4}\left|J_{k-i}-J_{k-i-1}\right|/\left|J_k\right|\le\varepsilon,\ \beta\ge 2^{10} \tag{28}$$

in the k-th iteration, where J_k is the objective value computed in the k-th iteration; ε is the tolerance chosen to be 1×10^{-3}.

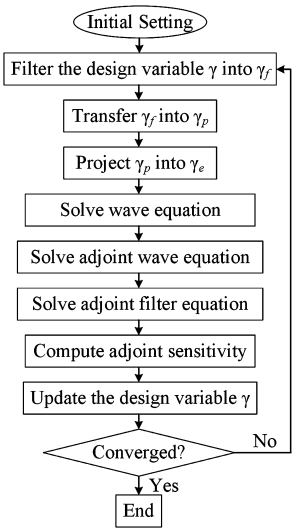

Fig. 2. Flowchart for the iterative solution procedure of the topology optimization problems.

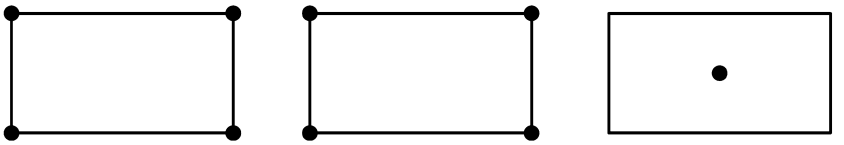

(a) Linear node element for H_{sz} and $\hat{H}_{sz}$.

(b) Linear node element for γ, γ_f and $\hat{\gamma}_f$.

(c) 0th-order discontinuous element for γ_e.

Fig. 3. The finite elements used in the topology optimization procedure for 2D electromagnetic waves.

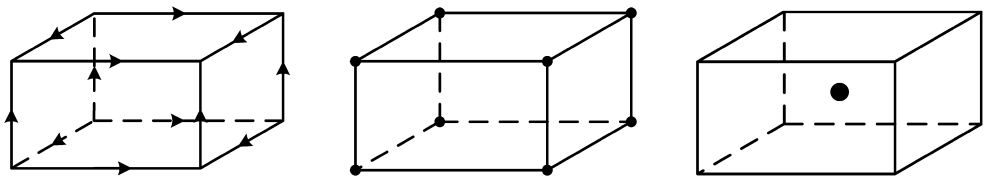

(a) Linear edge element for $\mathbf{E}_s$ and $\hat{\mathbf{E}}_s$.

(b) Linear nodal element for γ, γ_f and $\hat{\gamma}_f$.

(c) 0th-order discontinuous element for γ_e.

Fig. 4. The finite elements used in the topology optimization procedure for 3D electromagnetic waves.

In the iterative procedure, the numerical solution of PDEs are implemented based on finite element method [40,55]. The 2D wave equation, the filter equation and the corresponding adjoint equations are solved using the standard Galerkin finite element method; the 3D wave equation and the corresponding adjoint equation are solved using the edge element-based finite element method with linear edge elements [47,48]. It is noted that the original wave equations (1) and (2) are solved instead of the coupled equations for the split variables, because the sole destination of splitting operation is to derive the Fréchet differentiability during the adjoint analysis.

All of the finite element method-based numerical solutions and integrations are carried out in the commercial software COMSOL Multiphysics (www.comsol.com), based on the software's basic PDE module. For details on the setting of the *PDE Modes* and numerical integrations, one can refer to [49,50]. In the optimization procedures for the 2D problems, the magnetic field, design variable and filtered design variable are interpolated using linear node elements (Fig. 3a); and the projected design variable is interpolated using 0th-order discontinuous elements (Fig. 3b). In the optimization procedure for the 3D problems, the electric field is interpolated using linear edge elements (Fig. 4a); the design variable and filtered design variable is interpolated using linear nodal elements (Fig. 4b); the filtered design variable is converted to piecewise form by interpolating the piecewise design variable using 0th-order discontinuous elements (Fig. 4c), where P_n in equation (10) is set to be the space taken up by the finite elements. All the computation were performed on a DELL workstation (DELL PRECISION TOWER 7910, Intel Xeon CPU E5-2699 @ 2.30 GHz, RAM 128 GB).

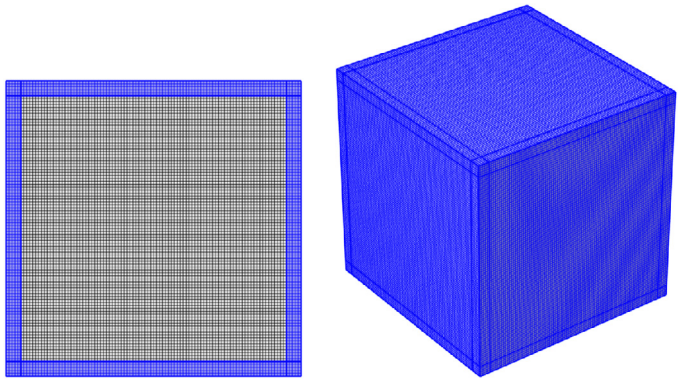

(a) 2D PMLs (b) 3D PMLs

Fig. 5. The PMLs marked in blue color and discretized by 5 layers of elements respectively for the 2D and 3D cloaks. (For interpretation of the references to color in this figure, the reader is referred to the web version of this article.)

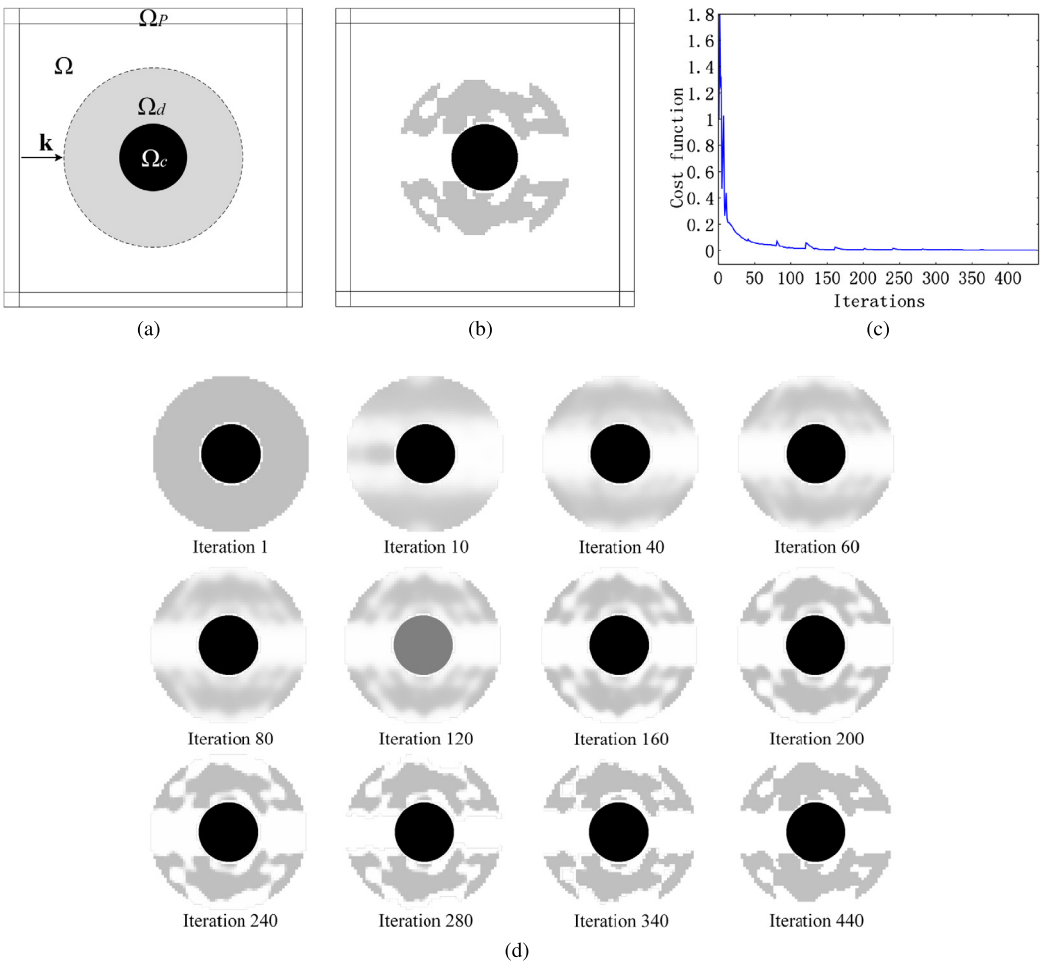

Fig. 6. (a) Sketch for the topology optimization of 2D dielectric cloak, where **k** is the wave vector of the incident wave; (b) structural topology of the 2D dielectric cloak for the incident wave with frequency 1×10^9 Hz and wave vector in positive x-axis; (c) convergent histories of the cost function, which is the normalized scattering field energy in the exterior of the 2D cloak; (d) snapshots for the evolutionary progress of the structural topology. The cost of CPU time is 1.20 h.

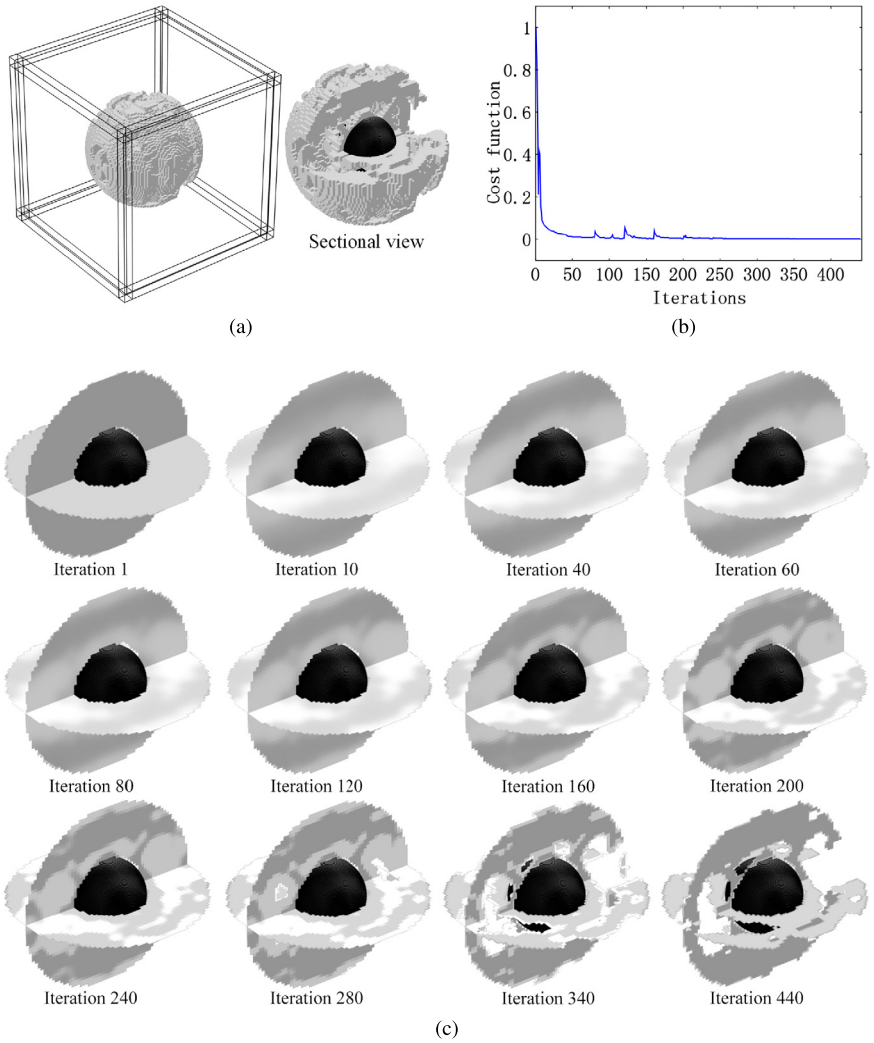

Fig. 7. (a) Structural topology of the 3D dielectric cloak for the incident wave with frequency 1×10^9 Hz and wave vector in positive x-axis; (b) convergent histories of the cost function, which is the normalized scattering field energy in the exterior of the 3D cloak; (c) snapshots for the evolutionary progress of the structural topology, where the structural topology is presented in two perpendicular cross sections of the design domain. The cost of CPU time is 241.25 h.

4.1. Dielectric cloaks

Dielectric cloak has been investigated using topology optimization by minimizing the scattering field energy around the cloak [5,6]. In these researches, the sensitivity analysis is implemented based on the Gâteaux differentiability of the conjugate operator. And the infinite space is truncated by the first order scattering boundary condition. As specified in [40], the first order scattering boundary condition has reflection, and this causes the relatively lower computational accuracy compared with truncating the infinite space by PMLs. In this section, the dielectric cloak is investigated using the sensitivity analysis approach with Fréchet differentiability, and the PMLs are used to achieve the scattering boundary. The cloaked object is set to be a 2D-circular or 3D-spherical conductor with high conductivity ($\epsilon_r = -1 \times 10^4 j$). The incident wave is set to be the uniform plane wave in free space, with frequency 1×10^9 Hz ($\lambda = 0.3$ m), wave vector in positive x-axis and polarization in z-axis. The computational domain is set to be square or cube with side length equal to 6-fold of the incident wavelength, respectively for the 2D and 3D cases; and it is enclosed by the PMLs with thickness equal to 1/3-fold of the incident wavelength. The conductor is localized at the center of the computational domain, and its radius of the conductor is 3/4-fold of the incident wavelength. The design domain is the 2D-ring or 3D-shell around the conductor, and the exterior radius of the design domain is 5/2-fold of the incident wavelength. The material of the cloak is the dielectrics with relative permittivity 2.25. The objective is to minimize the normalized scattering electric field energy in the exterior of the cloak

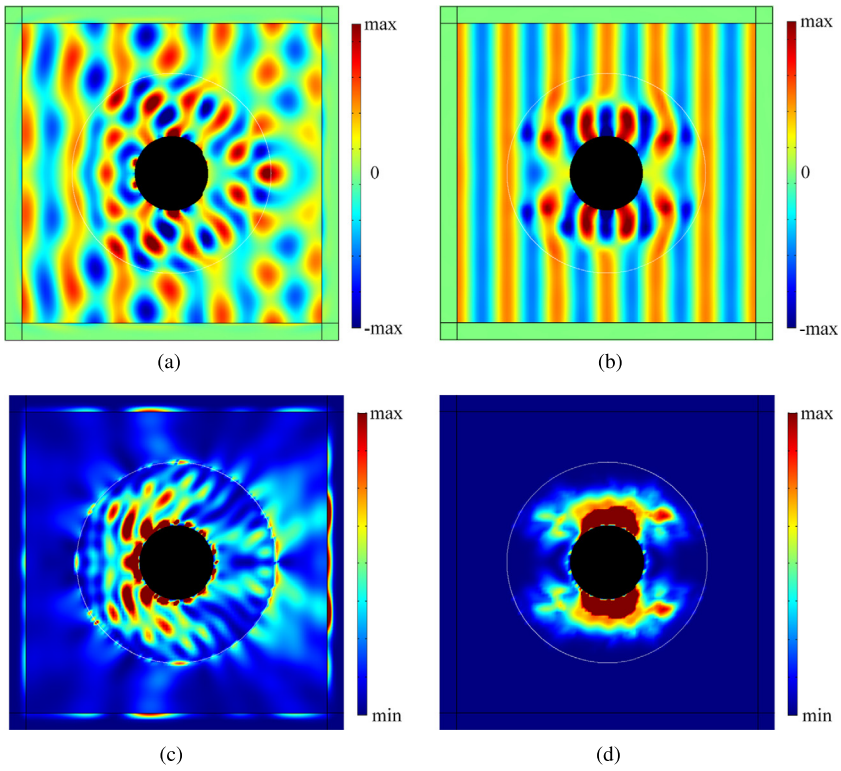

Fig. 8. (a) TM field around the design domain fully filled with dielectrics; (b) TM field around the derived 2D cloak; (c) energy of the TM field around the design domain fully filled with dielectrics; (d) energy of the TM field around the derived 2D cloak.

$$J = \frac{1}{J_0} \int_{\Omega \setminus (\Omega_d \cup \Omega_c)} \mathbf{E}_s \cdot \mathbf{E}_s^* \, \mathrm{d}\Omega \tag{29}$$

where J_0 is the norm square of the scattering electric field in the exterior of the design domain fully filled by the dielectrics; Ω is the computational domain; Ω_d is the design domain; Ω_c is the cloaked conductor domain; $\mathbf{E}_s$ is the scattering electric field, calculated to be $\frac{1}{j\epsilon_r\epsilon_0\omega}\nabla \times (0, 0, H_{sz})$ in the 2D cases.

The computational domains are discretized by 80×80 square elements and $80 \times 80 \times 80$ cube elements respectively for the 2D and 3D cases, where 5 layers of elements are used to discretize the PMLs (Fig. 5). For the 2D case, the topology optimization problem is sketched in Fig. 6a. By numerically implementing the topology optimization procedure with the derived self-consistent adjoint sensitivity, the 2D and 3D dielectric cloaks are derived as shown in Figs. 6b and 7a. Convergent histories of the cost functions are plotted in Figs. 6c and 7b. Snapshots for the evolutionary progress of the structural topology are shown in Figs. 6d and 7c. From the convergent histories of the cost functions and snapshots for the evolutionary progress of the structural topology, one can confirm the robustness of the self-consistent adjoint sensitivity-based optimization procedure for dielectric material topology. In the initial of the numerical procedure, the design domains are fully filled by the used dielectrics; the conductor enclosed with the dielectrics scatters the incident field as shown in Fig. 8a with the corresponding scattering field energy shown in Fig. 8c, for the 2D case; and the scattering field and corresponding scattering field energy are shown in Figs. 9a and 9c, for the 3D case. The adjoint sensitivity at the initial distribution of the design variable is checked using the finite difference computation for the 2D case, where the discretized design variable is perturbed by the variation 1×10^{-4} (Fig. 10). From finite difference check, the reasonability of the self-consistent adjoint sensitivity can be confirmed. With the derived cloaks, the scattering fields are weakened and the scattering field energy is prohibited effectively in the surrounding of the cloaks (Figs. 8b and 8d, Figs. 9b and 9d). Then the incident fields propagate with small disturbance and matched phase, and the cloaking effect of the derived dielectric structures is achieved as shown in Figs. 8b and 9b for detecting the fields behind the enclosed conductors. In addition, the incident waves with different phases have been tested respectively in this section for the numerical examples, and the same structural topology is derived. This verifies the effect of the self-consistent adjoint sensitivity on avoiding the incident wave-phase dependence of the derived dielectric structure topology.

To further demonstrate the self-consistency of the adjoint sensitivity derived by splitting the complex variables into the corresponding real and imaginary parts, the self-inconsistent adjoint sensitivity and the incident wave-phase dependence of the derived structure topology are computed for the 2D dielectric cloak. Without splitting the complex variables and according to the reference [36], the terms $-j\frac{\partial A}{\partial Im(H_{sz})}\phi$ and $-j\frac{\partial A}{\partial \nabla Im(H_{sz})} \cdot \nabla\phi$ are removed from the integral in equation (22),

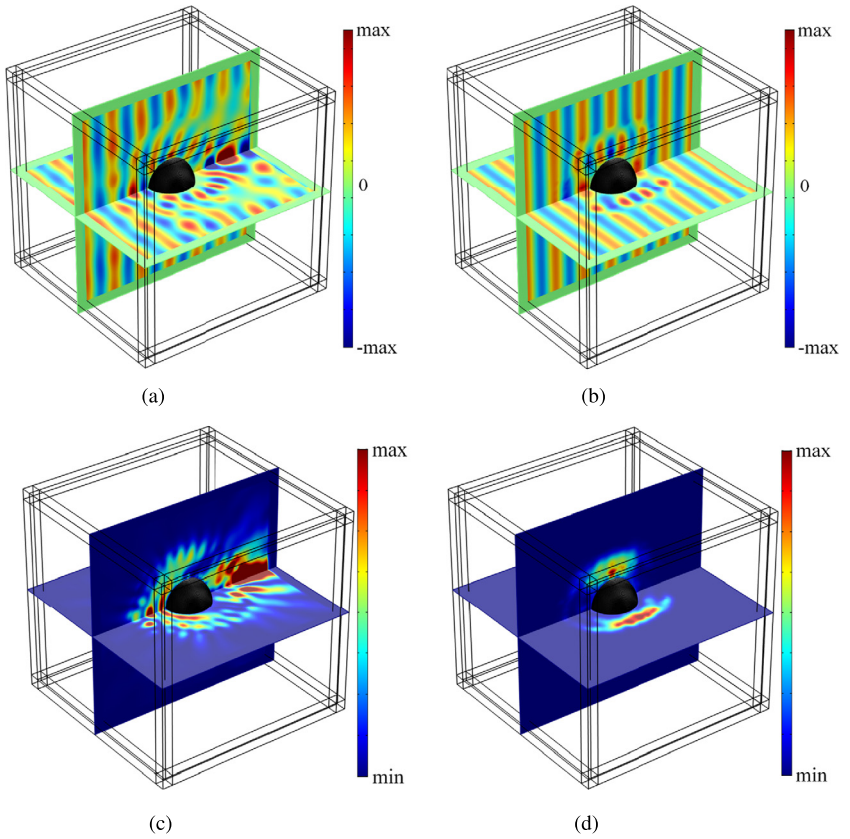

Fig. 9. (a) Electric field around the design domain fully filled with dielectrics; (b) electric field around the derived 3D cloak; (c) energy of the electric field around the design domain fully filled with dielectrics; (d) energy of the electric field around the derived 3D cloak.

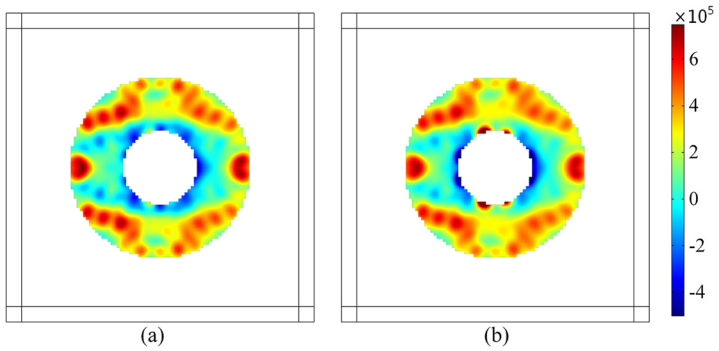

Fig. 10. (a) The self-consistent adjoint sensitivity for the 2D cloak computed by equation (24) at the initial distribution of the design variable; (b) the adjoint sensitivity for the 2D cloak computed by the finite difference method at the initial distribution of the design variable, where the perturbation 1×10^{-4} is imposed on the discretized design variable.

and the second and third terms in the bracket of equation (23) are replaced by $\frac{\partial \epsilon_r^{-1}}{\partial \gamma_p} \frac{\partial \gamma_p}{\partial \gamma_e} \nabla (H_{sz} + H_{iz}) \cdot \nabla \hat{H}_{sz}^*$; sequentially, the real-part extraction operator is imposed on the term $\frac{\partial A}{\partial \gamma} - \hat{\gamma}_f$ of the adjoint sensitivity in equation (24). With the same parameter setting, the topology optimization problem is solved for the incident wave $e^{-j\omega x + \phi_p}$, with x and ϕ_p respectively representing the horizontal coordinate and phase. It is valuable to note that $e^{-j\omega x + \phi_p}$ expresses the same wave, when only ϕ_p varies. Therefore, the derived structural topology should be independent on ϕ_p. By setting different values for ϕ_p in $[0, \pi]$, different cloak topologies are derived as shown in Figs. 11a–e, compared with the one in Fig. 11f derived by the self-consistent adjoint sensitivity; from the comparison of the cloak topologies shown in Fig. 11, one can confirm the phase-dependence problem of the self-inconsistent adjoint sensitivity. The normalized scattering electric field energy are cross checked in Table 1, for the derived cloak topologies in Fig. 11. From the cross-check, one can confirm optimality of the cloak topology derived using the self-consistent adjoint sensitivity. Snapshots for the evolution of the adjoint sensitivity are

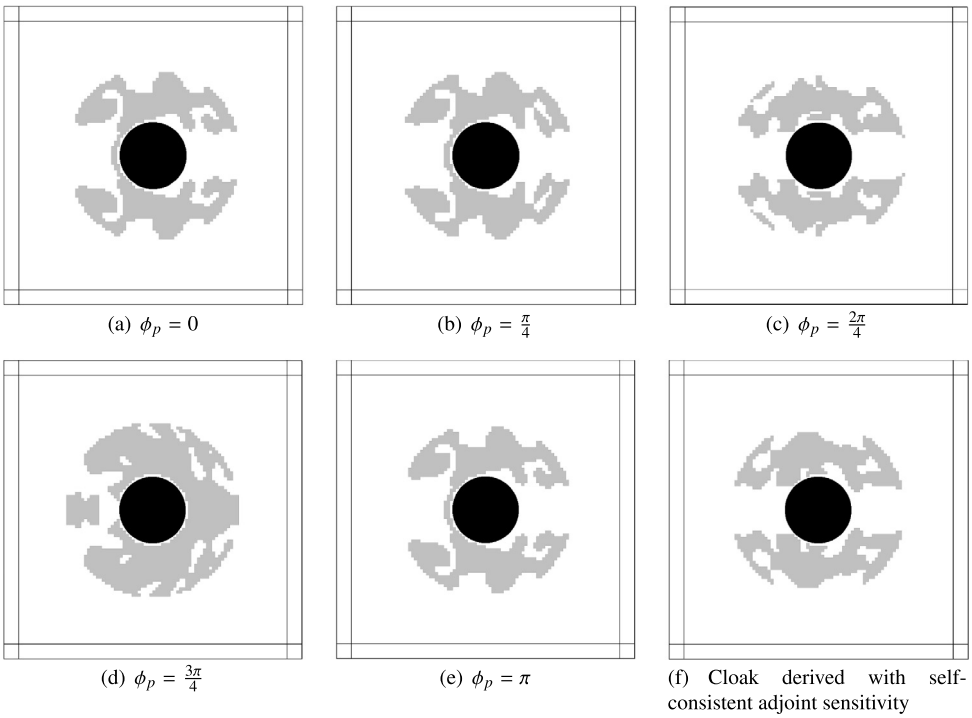

(a) $\phi_p = 0$ (b) $\phi_p = \frac{\pi}{4}$ (c) $\phi_p = \frac{2\pi}{4}$

(d) $\phi_p = \frac{3\pi}{4}$ (e) $\phi_p = \pi$ (f) Cloak derived with self-consistent adjoint sensitivity

Fig. 11. (a–e) Structural topologies of the 2D dielectric cloak derived with self-inconsistent adjoint sensitivity, for the incident wave with different phases; (f) structural topologies of the 2D dielectric cloak derived with self-consistent adjoint sensitivity.

Table 1
Cross-check of the normalized scattering electric field energy for the derived cloak topologies in Fig. 11, where the scattering electric field energy is normalized by the scattering electric field in the exterior of the design domain fully filled by the dielectrics.

Fig. 11a	Fig. 11b	Fig. 11c	Fig. 11d	Fig. 11e	Fig. 11f
3.3254×10^{-2}	5.4832×10^{-2}	9.5631×10^{-2}	1.2160×10^{-1}	7.1918×10^{-2}	3.9263×10^{-3}

shown in Fig. 12 respectively for the cloak topologies in Figs. 11a and 11f, where the imaginary part of adjoint sensitivity is non-zero in Fig. 12a and it is invariably zero in Fig. 12b; from the comparison of the snapshots for the adjoint sensitivity, one can confirm the self-consistency of the adjoint sensitivity derived by splitting the complex variables. The convergent histories of the cost function are plotted and compared in Fig. 13 for the derived cloak topologies in Figs. 11a–f, from which the accuracy of the self-consistent adjoint sensitivity and the optimality of the derived structural topology can be further confirmed by comparison.

To demonstrate the performance of self-consistent adjoint sensitivity on the refined mesh, the mesh used to discretize the computational domain for the 2D dielectric cloak is refined with 160×160 square elements. With the same parameter setting, the structural topology is derived as shown in Fig. 14b, and the convergent histories of the cost function are plotted in Fig. 14c. Compared with the result derived with the mesh of 80×80 square elements (Fig. 14a), it can be concluded that reasonable mesh refinement is helpful for the enhancement of the structural resolution of the derived dielectric topology.

4.2. LSPR nanostructures

Localized surface plasmon resonances (LSPRs) are the strong interaction between nanostructures and visible light through the resonant excitations of collective oscillations of conduction electrons. In LSPRs, the local electromagnetic field near the nanostructure can be many orders of magnitude higher than the incident field, and the incident field around the resonant-peak wavelength is scattered strongly; the enhanced electric field is confined within only a tiny region of the nanometer length scale near the surface of the nanostructures and decays significantly thereafter [56]. Surface-enhanced Raman spectroscopy (SERS) is one typical application of LSPRs [57]. In this section, the computational design is carried out for the metallic nanostructures of LSPRs using the self-consistent adjoint sensitivity-based topology optimization procedure. The material for the nanostructure is set to be the noble metal Au (gold) with complex relative permittivity referred to [58]. The computational domain is set to be 2D-square and 3D-cube with side length equal to 1/2-fold of the incident wavelength, and it is enclosed by the PMLs with thickness equal to 1/20-fold of the incident wavelength. The incident wave is set to be the uniform plane wave in free space, with frequency 3.75×10^{14} Hz ($\lambda = 800$ nm), wave vector in

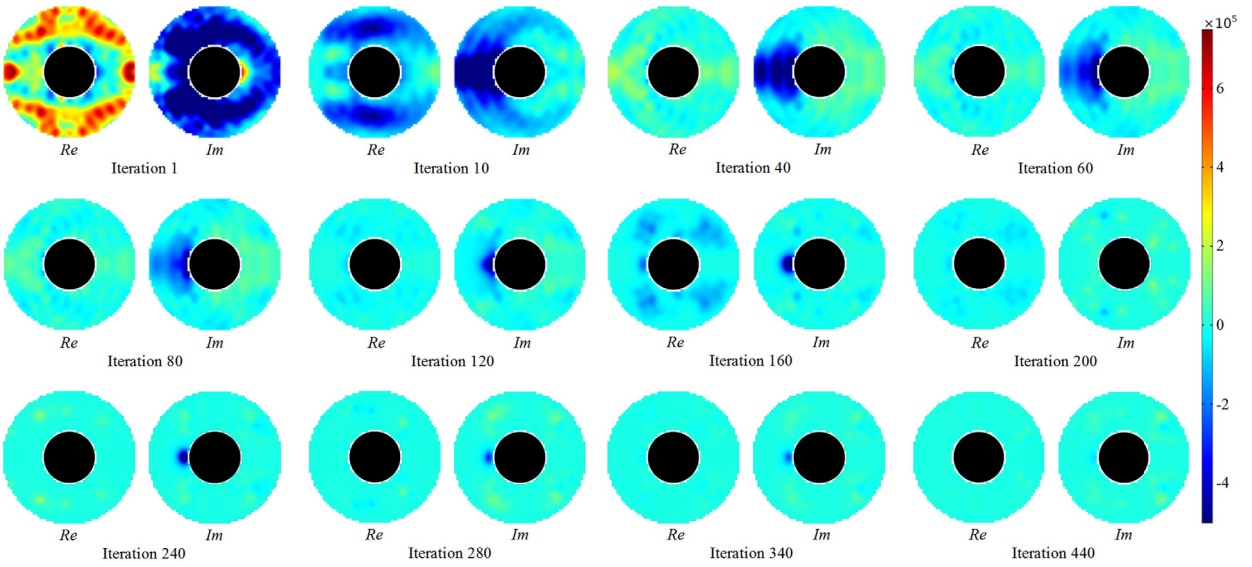

(a)

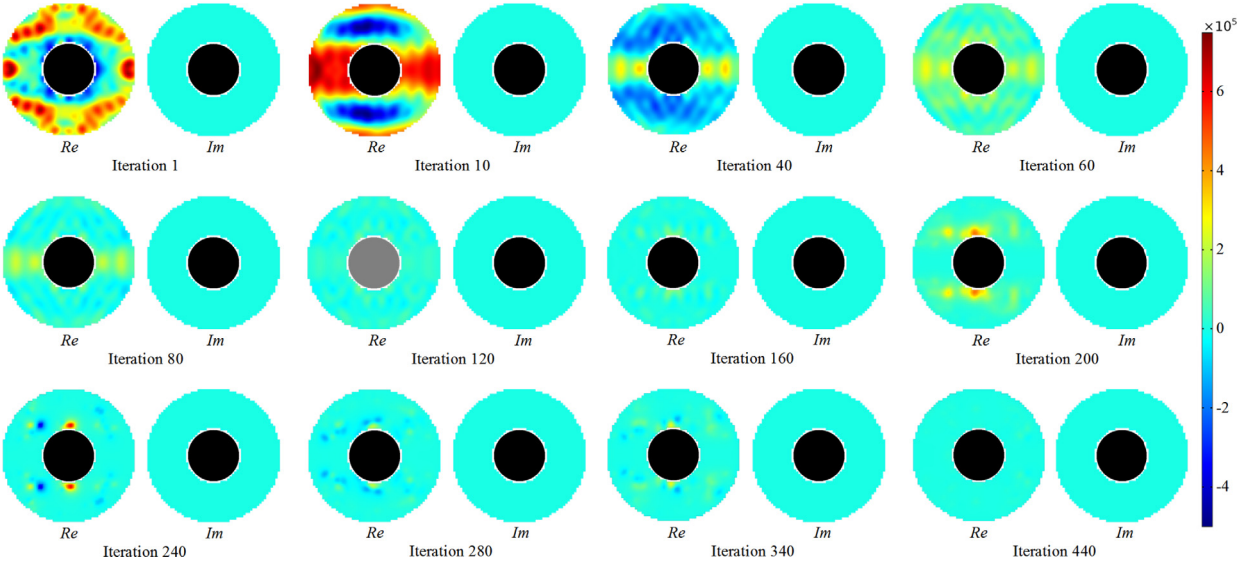

(b)

Fig. 12. (a) Snapshots for the self-inconsistent adjoint sensitivity in the evolution procedure of the structural topology in Fig. 11a; (b) snapshots for the self-consistent adjoint sensitivity in the evolution procedure of the structural topology in Fig. 11f.

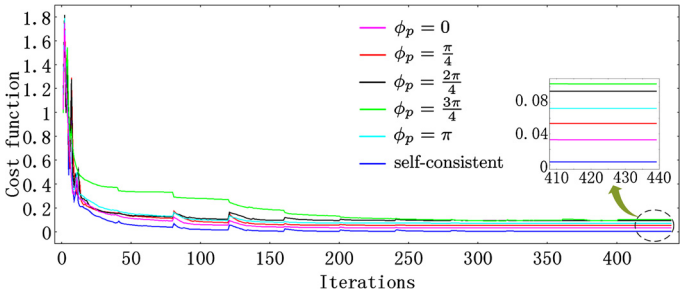

Fig. 13. Convergent histories for the structural topologies shown in Fig. 11.

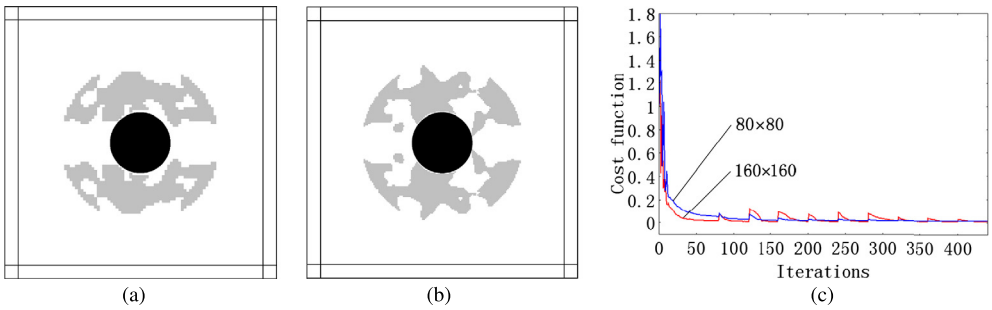

Fig. 14. (a) Structural topology of the 2D dielectric cloak derived with the mesh of 80×80 square elements; (b) structural topology of the 2D dielectric cloak derived with the mesh of 160×160 square elements; (c) convergent histories of the structural topologies in (a) and (b). The cost of CPU time is 2.17 h for the result in (b).

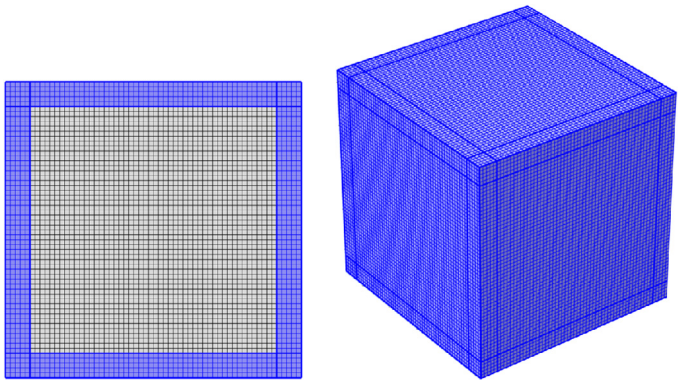

Fig. 15. The PMLs marked in blue color and discretized by 5 layers of elements respectively for the 2D and 3D metal nanostructures for LSPRs. (For interpretation of the references to color in this figure, the reader is referred to the web version of this article.)

positive x-axis and polarization in z-axis. The design domain is set to be 2D-circle and 3D-sphere localized at the center of the design domain, and the radius of the design domain is 1/5-fold of the incident wavelength. The desired LSPR is at the center of the design domain. The strength of LSPRs is measured by the enhancement factor defined at the specified position. Therefore, the cost function can be set to maximize the normalized enhancement factor expressed as

$$J = \frac{1}{J_0} \int_{\Omega} \mathbf{E} \cdot \mathbf{E}^* \delta \left(\mathbf{x} - \mathbf{x}_c \right) \mathrm{d}\Omega \tag{30}$$

where $J_0 = \int_{\Omega} \mathbf{E}_i \cdot \mathbf{E}_i^* \delta \left(\mathbf{x} - \mathbf{x}_c \right) \mathrm{d}\Omega$ is the 2-norm of the electric field at the LSPR position; Ω is the computational domain; $\mathbf{x}_c$ is the desired LSPR position, set to be the center of the design domain; $\mathbf{E}$ is the electric field, calculated to be $\frac{1}{j\epsilon_r \epsilon_0 \omega} \nabla \times (0, 0, H_z)$ in the 2D case.

The computational domains are discretized by 50×50 square elements and $50 \times 50 \times 50$ cube elements respectively for the 2D and 3D cases, where 5 layers of elements are used to discretize the PMLs (Fig. 15). For the 2D case, the topology optimization problem is sketched in Fig. 16a. By numerically implementing the topology optimization procedure with the derived self-consistent adjoint sensitivity, the 2D and 3D LSPR nanostructures are derived as shown in Figs. 16b and 18a. Convergent histories of the cost function are plotted in Figs. 16c and 18b. Snapshots for the evolutionary progress of the structural topology are shown in Figs. 16d and 18c. From the convergent histories of the cost function and snapshots for the evolutionary progress of the structural topology, one can confirm the robustness of the self-consistent adjoint sensitivity-based optimization procedure for metallic material topology. In the initial of the numerical procedure, the design domains are set to be free space. To maximize the enhancement factor of the electric field at the center of the computational domain, the topology optimization procedure nucleates the noble metal-based nanostructure as shown in Figs. 16b and 18a, respectively for the 2D and 3D cases. The electric field distribution and corresponding enhancement factor around the derived 2D and 3D nanostructures are shown in Figs. 17 and 19, respectively. In the geometrical configurations of the derived 2D and 3D material topology, the pit configurations are formed at the neighboring of the desired LSPR position to increase the charge density, which is proportional to the strength of the electric field. The strong charge density can be confirmed from the density and length of the arrows for the electric field shown in Figs. 17b and 19b. With the strong charge density, the two tips are coupled together, and this achieves the LSPR effect. In addition, the incident waves with different phases

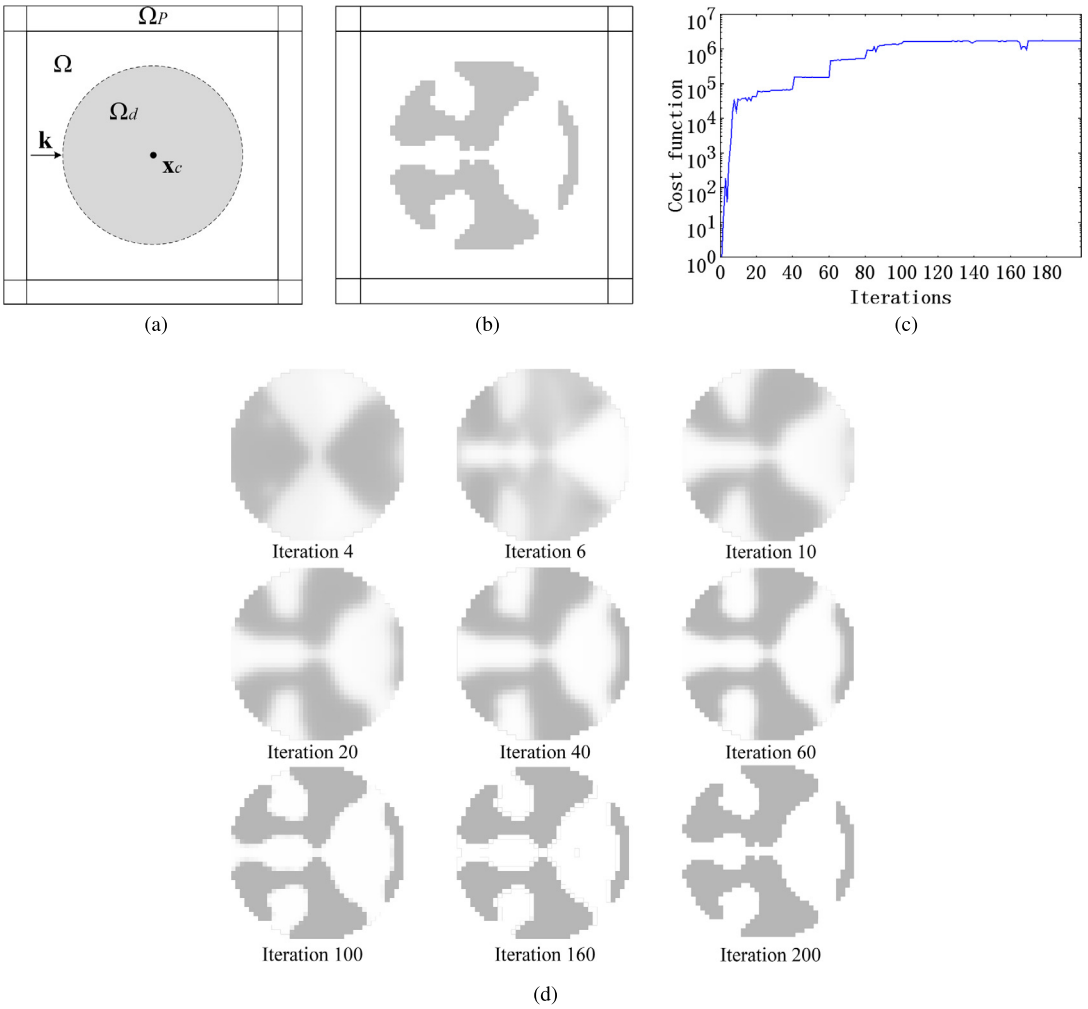

Fig. 16. (a) Sketch for the topology optimization of 2D metal nanostructure with LSPR at the position $\mathbf{x}_c$, where $\mathbf{k}$ is the wave vector of the incident wave; (b) structural topology of the 2D metal nanostructure for the incident wave with frequency 3.75×10^{14} Hz and wave vector in positive x-axis; (c) convergent histories of the cost function, which is the enhancement factor of the electric field at the specified LSPR position at the center of the computational domain; (d) snapshots for the evolutionary progress of the 2D structural topology. The cost of CPU time is 0.92 h.

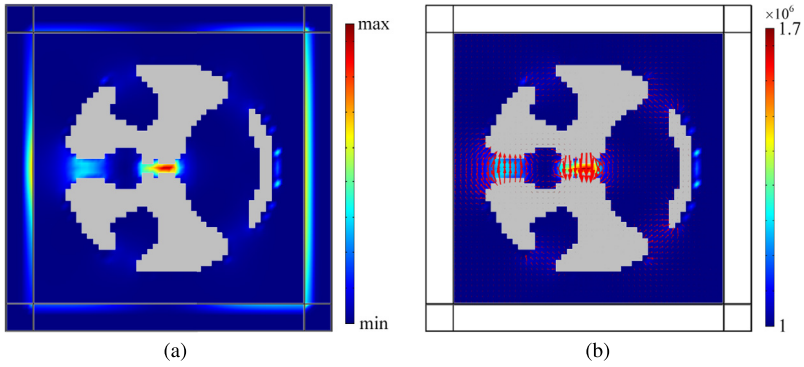

Fig. 17. (a) Electric field energy distribution around the derived 2D metal nanostructure; (b) enhancement factor distribution of the electric field around the derived 2D metal nanostructure, where the proportional arrows are used to illuminate the strength and direction of the electric field.

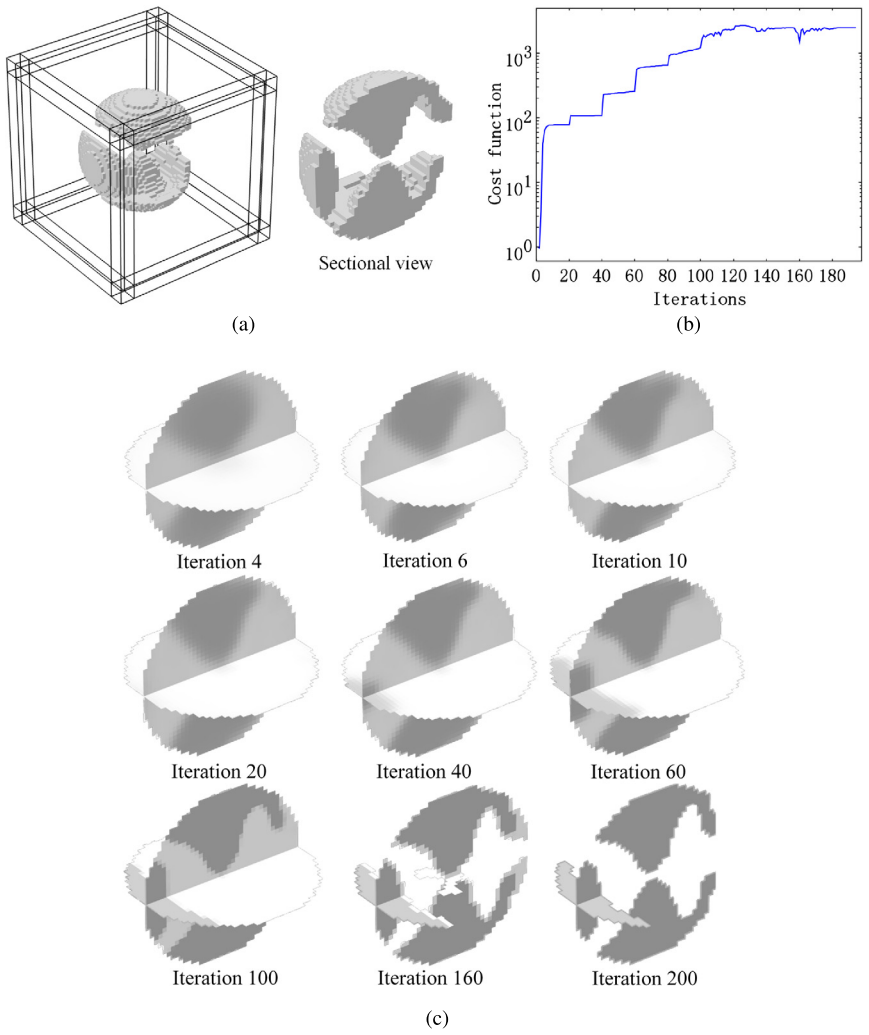

Fig. 18. (a) Structural topology of the 3D metal nanostructure for the incident wave with frequency 3.75×10^{14} Hz and wave vector in positive x-axis; (b) convergent histories of the cost function, which is the enhancement factor of the electric field at the specified LSPR position at the center of the computational domain; (c) snapshots for the evolutionary progress of the 3D structural topology, where the structural topology is presented in two perpendicular cross sections of the design domain. The cost of CPU time is 24.08 h.

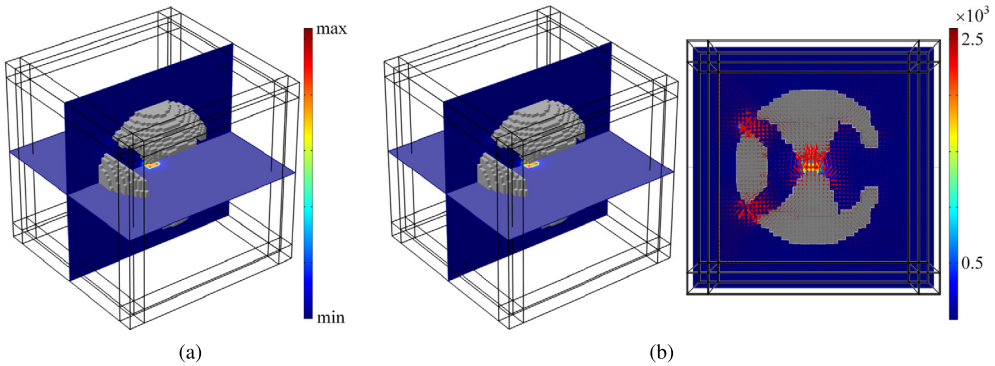

Fig. 19. (a) Electric field energy distribution in two perpendicular cross sections of the derived 3D metal nanostructure; (b) enhancement factor distribution of the electric field in two perpendicular cross sections of the derived 3D metal nanostructure, where the proportional arrows are used to illuminate the strength and direction of the electric field.

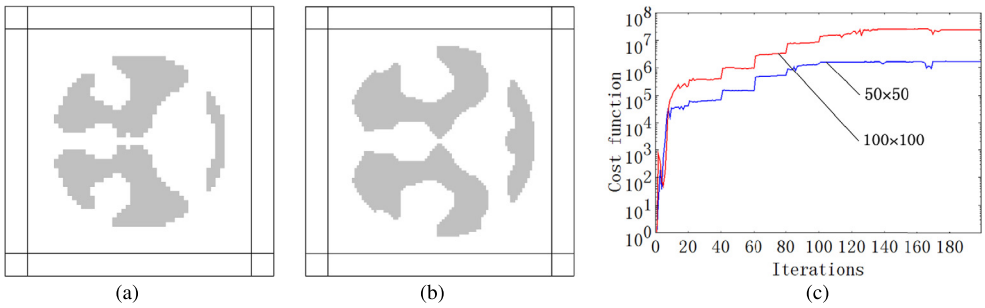

Fig. 20. (a) Structural topology of the 2D metal nanostructure derived with the mesh of 50×50 square elements; (b) structural topology of the 2D metal nanostructure derived with the mesh of 100×100 square elements; (c) convergent histories of the structural topologies in (a) and (b). The cost of CPU time is 2.02 h for the result in (b).

have also been tested in this section for the numerical examples, and the same structural topology is derived. This verifies the effect of the self-consistent adjoint sensitivity on avoiding the incident wave-phase dependence of the derived metallic structure topology.

To further demonstrate the performance of self-consistent adjoint sensitivity on the refined mesh, the mesh used to discretize the computational domain for 2D metal nanostructure is refined with 100×100 square elements. With the same parameter setting, the structural topology is derived as shown in Fig. 20b, and the convergent histories of the cost function are plotted in Fig. 20c. Compared with the result derived with the mesh of 50×50 square elements (Fig. 20a), it can be concluded that mesh refinement can effectively enhance the reasonability and resolution of the derived plasmonic topology.

There is a stepped fashion in the plots of the convergent histories of the cost functions in this article. The stepped fashion occurs, when the projection parameter β (in equation (11)) is updated. In equation (11), the updating of the projection parameter can result in a sudden change of the derivative of γ_p to γ_e. Therefore, the updating of this parameter can make the gradient of the physical density γ_p change suddenly. And this sudden change of the physical density can result in a step-shape change of the cost-function value in the iterative procedure, as shown in the plots of the convergent histories.

5. Conclusions

This article has presented the self-consistent adjoint analysis for the topology optimization of electromagnetic waves. By splitting the two dimensional or three dimensional wave equations into coupled equations respectively for the real parts and imaginary parts of the field variables in the frequency domain, the topology optimization problems are transformed into the forms defined on real functional spaces instead of complex ones; and the Fréchet differentiability of the cost functions, containing conjugate of the field variables, is ensured respectively to the real and imaginary parts of the field variable. Therefore, the adjoint sensitivity is derived with self-consistency, which can ensure the real-value property of the design variable during the iterative updating procedure. With the self-consistent adjoint sensitivity, the unreasonable dependence on the phase of the incident wave is prevented for the derived structural topology. Because the infinite free space is truncated by perfectly matched layers instead of first order scattering boundary condition, this article has also presented the mathematical formulation for the adjoint analysis of optimization problems constrained by the wave equations with perfectly matched layers. The robustness of the self-consistent adjoint sensitivity has been demonstrated by several two dimensional and three dimensional numerical tests, which are implemented respectively for the topology optimization with dielectric and metallic materials.

Acknowledgements

This work is supported by the National Natural Science Foundation of China (No. 51405465), a Guest Professor Fellowship at the Karlsruhe Institute of Technology (KIT) by the DFG Metacoil project (KO 1883/20-1), the National High Technology Program of China (No. 2015AA042604), and Science and Technology Development Plan of Changchun City (No. 15SS12). J. G. Korvink is supported by an ERC Senior Grant (NMCEL, 290586) and by the Karlsruhe School of Optics and Photonics (KSOP). J. G. Korvink is also supported through the Cluster of Excellence BrainLinks-BrainTools (DFG, grant no. EXC 1086). The authors are grateful to Prof. K. Svanberg for his supplying the MMA codes; they are also grateful to the reviewers' kind attention and valuable suggestions.

Appendix A

A.1. Adjoint analysis of topology optimization problem for 2D electromagnetic waves

Based on the Lagrangian multiplier-based adjoint method, the augmented Lagrangian for the topology optimization problem in equation (20) can be written to be

$$
\begin{aligned}
\hat{J} = & \int_{\Omega} A\left(H_{sz}^{R}, H_{sz}^{I}, \nabla H_{sz}^{R}, \nabla H_{sz}^{I}, \gamma_p; \gamma\right) - \left(\epsilon_r^{-1}\right)^{R} \nabla\left(H_{sz}^{R} + H_{iz}^{R}\right) \cdot \nabla \hat{H}_{sz}^{R} + \left(\epsilon_r^{-1}\right)^{I} \nabla\left(H_{sz}^{I} + H_{iz}^{I}\right) \cdot \nabla \hat{H}_{sz}^{R} \\
& + k_0^2 \mu_r \left(H_{sz}^{R} + H_{iz}^{R}\right) \hat{H}_{sz}^{R} - \left(\epsilon_r^{-1}\right)^{I} \nabla\left(H_{sz}^{R} + H_{iz}^{R}\right) \cdot \nabla \hat{H}_{sz}^{I} - \left(\epsilon_r^{-1}\right)^{R} \nabla\left(H_{sz}^{I} + H_{iz}^{I}\right) \cdot \nabla \hat{H}_{sz}^{I} \\
& + k_0^2 \mu_r \left(H_{sz}^{I} + H_{iz}^{I}\right) \hat{H}_{sz}^{I} \, \mathrm{d}\Omega - \int_{\Omega_P} \left(\epsilon_r^{-1}\right)^{R} \left(\mathbf{T}\nabla H_{sz}^{R}\right) \cdot \left(\mathbf{T}\nabla \hat{H}_{sz}^{R}\right) |\mathbf{T}|^{-1} + \left(\epsilon_r^{-1}\right)^{I} \left(\mathbf{T}\nabla H_{sz}^{R}\right) \cdot \left(\mathbf{T}\nabla \hat{H}_{sz}^{I}\right) |\mathbf{T}|^{-1} \\
& - k_0^2 \mu_r H_{sz}^{R} \hat{H}_{sz}^{R} |\mathbf{T}| - \left(\epsilon_r^{-1}\right)^{I} \left(\mathbf{T}\nabla H_{sz}^{I}\right) \cdot \left(\mathbf{T}\nabla \hat{H}_{sz}^{R}\right) |\mathbf{T}|^{-1} + \left(\epsilon_r^{-1}\right)^{R} \left(\mathbf{T}\nabla H_{sz}^{I}\right) \cdot \left(\mathbf{T}\nabla \hat{H}_{sz}^{I}\right) |\mathbf{T}|^{-1} \\
& - k_0^2 \mu_r H_{sz}^{I} \hat{H}_{sz}^{I} |\mathbf{T}| \, \mathrm{d}\Omega + \int_{\Omega_d} r^2 \nabla \gamma_f \cdot \nabla \hat{\gamma}_f + \gamma_f \hat{\gamma}_f - \gamma \hat{\gamma}_f \, \mathrm{d}\Omega
\end{aligned} \tag{31}
$$

where $\hat{H}_{sz}^{R} \in \mathcal{H}(\Omega \cup \Omega_P)$ with $\hat{H}_{sz}^{R} = 0$ on Γ_D, $\hat{H}_{sz}^{I} \in \mathcal{H}(\Omega \cup \Omega_P)$ with $\hat{H}_{sz}^{I} = 0$ on Γ_D, and $\hat{\gamma}_f \in \mathcal{H}(\Omega_d)$ are the adjoint variables of $H_{sz}^{R} \in \mathcal{H}(\Omega \cup \Omega_P)$, $H_{sz}^{I} \in \mathcal{H}(\Omega \cup \Omega_P)$, and $\gamma_f \in \mathcal{H}(\Omega_d)$, respectively; $\mathcal{H}(\Omega \cup \Omega_P)$ and $\mathcal{H}(\Omega_d)$ are the first order Hilbert spaces for the real functions defined on $\Omega \cup \Omega_P$ and Ω_d, respectively; $\mathbf{T}$ is the transformation matrix in equation (5). The first order variational of the augmented Lagrangian to the field variables and design variable is

$$
\begin{aligned}
\delta \hat{J} = & \int_{\Omega} \frac{\partial A}{\partial H_{sz}^{R}} \delta H_{sz}^{R} + \frac{\partial A}{\partial H_{sz}^{I}} \delta H_{sz}^{I} + \frac{\partial A}{\partial \nabla H_{sz}^{R}} \cdot \nabla \delta H_{sz}^{R} + \frac{\partial A}{\partial \nabla H_{sz}^{I}} \cdot \nabla \delta H_{sz}^{I} \, \mathrm{d}\Omega + \sum_{n=1}^{N} \frac{1}{V_n} \int_{P_n} \frac{\partial A}{\partial \gamma_p} \frac{\partial \gamma_p}{\partial \gamma_e} \delta \gamma_f \, \mathrm{d}\Omega \\
& + \int_{\Omega_d} \frac{\partial A}{\partial \gamma} \delta \gamma \, \mathrm{d}\Omega + \int_{\Omega} - \left(\epsilon_r^{-1}\right)^{R} \nabla \delta H_{sz}^{R} \cdot \nabla \hat{H}_{sz}^{R} + \left(\epsilon_r^{-1}\right)^{I} \nabla \delta H_{sz}^{I} \cdot \nabla \hat{H}_{sz}^{R} + k_0^2 \mu_r \delta H_{sz}^{R} \hat{H}_{sz}^{R} \\
& - \left(\epsilon_r^{-1}\right)^{I} \nabla \delta H_{sz}^{R} \cdot \nabla \hat{H}_{sz}^{I} - \left(\epsilon_r^{-1}\right)^{R} \nabla \delta H_{sz}^{I} \cdot \nabla \hat{H}_{sz}^{I} + k_0^2 \mu_r \delta H_{sz}^{I} \hat{H}_{sz}^{I} \, \mathrm{d}\Omega \\
& - \int_{\Omega_P} \left(\epsilon_r^{-1}\right)^{R} \left[\mathbf{T}\left(\nabla \delta H_{sz}^{R}\right)\right] \cdot \left[\mathbf{T}\left(\nabla \hat{H}_{sz}^{R}\right)\right] |\mathbf{T}|^{-1} + \left(\epsilon_r^{-1}\right)^{I} \left[\mathbf{T}\left(\nabla \delta H_{sz}^{R}\right)\right] \cdot \left[\mathbf{T}\left(\nabla \hat{H}_{sz}^{I}\right)\right] |\mathbf{T}|^{-1} \\
& - k_0^2 \mu_r \delta H_{sz}^{R} \hat{H}_{sz}^{R} |\mathbf{T}| - \left(\epsilon_r^{-1}\right)^{I} \left(\mathbf{T}\nabla \delta H_{sz}^{I}\right) \cdot \left(\mathbf{T}\nabla \hat{H}_{sz}^{R}\right) |\mathbf{T}|^{-1} + \left(\epsilon_r^{-1}\right)^{R} \left(\mathbf{T}\nabla \delta H_{sz}^{I}\right) \cdot \left(\mathbf{T}\nabla \hat{H}_{sz}^{I}\right) |\mathbf{T}|^{-1} \\
& - k_0^2 \mu_r \delta H_{sz}^{I} \hat{H}_{sz}^{I} |\mathbf{T}| \, \mathrm{d}\Omega + \int_{\Omega_d} r^2 \nabla \delta \gamma_f \cdot \nabla \hat{\gamma}_f + \delta \gamma_f \hat{\gamma}_f - \delta \gamma \hat{\gamma}_f \, \mathrm{d}\Omega \\
& + \sum_{n=1}^{N} \frac{1}{V_n} \int_{P_n} - \frac{\partial \left(\epsilon_r^{-1}\right)^{R}}{\partial \gamma_p} \frac{\partial \gamma_p}{\partial \gamma_e} \nabla\left(H_{sz}^{R} + H_{iz}^{R}\right) \cdot \nabla \hat{H}_{sz}^{R} \delta \gamma_f + \frac{\partial \left(\epsilon_r^{-1}\right)^{I}}{\partial \gamma_p} \frac{\partial \gamma_p}{\partial \gamma_e} \nabla\left(H_{sz}^{I} + H_{iz}^{I}\right) \cdot \nabla \hat{H}_{sz}^{R} \delta \gamma_f \\
& - \frac{\partial \left(\epsilon_r^{-1}\right)^{I}}{\partial \gamma_p} \frac{\partial \gamma_p}{\partial \gamma_e} \nabla\left(H_{sz}^{R} + H_{iz}^{R}\right) \cdot \nabla \hat{H}_{sz}^{I} \delta \gamma_f - \frac{\partial \left(\epsilon_r^{-1}\right)^{R}}{\partial \gamma_p} \frac{\partial \gamma_p}{\partial \gamma_e} \nabla\left(H_{sz}^{I} + H_{iz}^{I}\right) \cdot \nabla \hat{H}_{sz}^{I} \delta \gamma_f \, \mathrm{d}\Omega
\end{aligned} \tag{32}
$$

where δH_{sz}^{R}, δH_{sz}^{I}, $\delta \gamma_f$ and $\delta \gamma$ are the first order variational of H_{sz}^{R}, H_{sz}^{I}, γ_f and γ, respectively. From the Kurash–Kuhn–Tucker condition of the partial differential equation constrained optimization problem [54], the first order variational of the augmented Lagrangian to the field variables satisfies

$$
\begin{aligned}
& \int_{\Omega} \frac{\partial A}{\partial H_{sz}^{R}} \delta H_{sz}^{R} + \frac{\partial A}{\partial \nabla H_{sz}^{R}} \cdot \nabla \delta H_{sz}^{R} - \left(\epsilon_r^{-1}\right)^{R} \nabla \delta H_{sz}^{R} \cdot \nabla \hat{H}_{sz}^{R} - \left(\epsilon_r^{-1}\right)^{I} \nabla \delta H_{sz}^{R} \cdot \nabla \hat{H}_{sz}^{I} + k_0^2 \mu_r \delta H_{sz}^{R} \hat{H}_{sz}^{R} \, \mathrm{d}\Omega \\
& - \int_{\Omega_P} \left(\epsilon_r^{-1}\right)^{R} \left[\mathbf{T}\left(\nabla \delta H_{sz}^{R}\right)\right] \cdot \left[\mathbf{T}\left(\nabla \hat{H}_{sz}^{R}\right)\right] |\mathbf{T}|^{-1} + \left(\epsilon_r^{-1}\right)^{I} \left[\mathbf{T}\left(\nabla \delta H_{sz}^{R}\right)\right] \cdot \left[\mathbf{T}\left(\nabla \hat{H}_{sz}^{I}\right)\right] |\mathbf{T}|^{-1} \\
& - k_0^2 \mu_r \delta H_{sz}^{R} \hat{H}_{sz}^{R} |\mathbf{T}| \, \mathrm{d}\Omega = 0
\end{aligned} \tag{33}
$$

$$
\begin{aligned}
& \int_{\Omega} \frac{\partial A}{\partial H_{sz}^{I}} \delta H_{sz}^{I} + \frac{\partial A}{\partial \nabla H_{sz}^{I}} \cdot \nabla \delta H_{sz}^{I} + \left(\epsilon_r^{-1}\right)^{I} \nabla \delta H_{sz}^{I} \cdot \nabla \hat{H}_{sz}^{R} - \left(\epsilon_r^{-1}\right)^{R} \nabla \delta H_{sz}^{I} \cdot \nabla \hat{H}_{sz}^{I} + k_0^2 \mu_r \delta H_{sz}^{I} \hat{H}_{sz}^{I} \, \mathrm{d}\Omega \\
& + \int_{\Omega_P} \left(\epsilon_r^{-1}\right)^{I} \left[\mathbf{T}\left(\nabla \delta H_{sz}^{I} \cdot \nabla \hat{H}_{sz}^{R}\right)\right] |\mathbf{T}|^{-1} - \left(\epsilon_r^{-1}\right)^{R} \left[\mathbf{T}\left(\nabla \delta H_{sz}^{I} \cdot \nabla \hat{H}_{sz}^{I}\right)\right] |\mathbf{T}|^{-1} \\
& + k_0^2 \mu_r \delta H_{sz}^{I} \hat{H}_{sz}^{I} |\mathbf{T}| \, \mathrm{d}\Omega = 0
\end{aligned} \tag{34}
$$

$$\int_{\Omega_d} r^2\nabla\delta\gamma_f\cdot\nabla\hat{\gamma}_f+\delta\gamma_f\hat{\gamma}_f+\sum_{n=1}^{N}\frac{1}{V_n}\int_{P_n}\frac{\partial A}{\partial\gamma_p}\frac{\partial\gamma_p}{\partial\gamma_e}\delta\gamma_f-\frac{\partial\left(\epsilon_r^{-1}\right)^R}{\partial\gamma_p}\frac{\partial\gamma_p}{\partial\gamma_e}\nabla\left(H_{sz}^R+H_{iz}^R\right)\cdot\nabla\hat{H}_{sz}^R\delta\gamma_f$$
$$+\frac{\partial\left(\epsilon_r^{-1}\right)^I}{\partial\gamma_p}\frac{\partial\gamma_p}{\partial\gamma_e}\nabla\left(H_{sz}^I+H_{iz}^I\right)\cdot\nabla\hat{H}_{sz}^R\delta\gamma_f-\frac{\partial\left(\epsilon_r^{-1}\right)^I}{\partial\gamma_p}\frac{\partial\gamma_p}{\partial\gamma_e}\nabla\left(H_{sz}^R+H_{iz}^R\right)\cdot\nabla\hat{H}_{sz}^I\delta\gamma_f \tag{35}$$
$$-\frac{\partial\left(\epsilon_r^{-1}\right)^R}{\partial\gamma_p}\frac{\partial\gamma_p}{\partial\gamma_e}\nabla\left(H_{sz}^I+H_{iz}^I\right)\cdot\nabla\hat{H}_{sz}^I\delta\gamma_f\,\mathrm{d}\Omega=0$$

And the adjoint sensitivity can be derived to be the first order variational of the augmented Lagrangian to the design variable

$$\delta\hat{J}=\int_{\Omega_d}\left(\frac{\partial A}{\partial\gamma}-\hat{\gamma}_f\right)\delta\gamma\,\mathrm{d}\Omega \tag{36}$$

Without losing the arbitrariness of δH_{sz}^R, δH_{sz}^I and $\delta\gamma_f$, one can set $\delta H_{sz}^R=\delta H_{sz}^I=\phi$ with $\forall\phi\in\mathcal{H}(\Omega\cup\Omega_P)$ and $\delta\gamma_f=\varphi$ with $\forall\varphi\in\mathcal{H}(\Omega_d)$. By substituting ϕ and φ into equations (33), (34) and (35), and adding equation (34) multiplied by $-j$ to equation (33), the adjoint equations for the topology optimization problem in equation (14) can be derived to be: find $\hat{H}_{sz}$ with $Re\left(\hat{H}_{sz}\right)\in\mathcal{H}(\Omega\cup\Omega_P)$, $Im\left(\hat{H}_{sz}\right)\in\mathcal{H}(\Omega\cup\Omega_P)$ and $\hat{H}_{sz}=0$ on Γ_D, satisfying

$$\int_{\Omega}\left(\frac{\partial A}{\partial Re\left(H_{sz}\right)}-j\frac{\partial A}{\partial Im\left(H_{sz}\right)}\right)\phi+\left(\frac{\partial A}{\partial\nabla Re\left(H_{sz}\right)}-j\frac{\partial A}{\partial\nabla Im\left(H_{sz}\right)}\right)\cdot\nabla\phi-\epsilon_r^{-1}\nabla\hat{H}_{sz}^*\cdot\nabla\phi$$
$$+k_0^2\mu_r\hat{H}_{sz}^*\phi\,\mathrm{d}\Omega+\int_{\Omega_P}-\epsilon_r^{-1}\left(\mathbf{T}\nabla\hat{H}_{sz}^*\right)\cdot\left(\mathbf{T}\nabla\phi\right)|\mathbf{T}|^{-1}+k_0^2\mu_r\hat{H}_{sz}^*\phi\,|\mathbf{T}|\,\mathrm{d}\Omega=0,\ \forall\phi\in\mathcal{H}(\Omega\cup\Omega_P) \tag{37}$$

find $\hat{\gamma}_f\in\mathcal{H}(\Omega_d)$ satisfying

$$\int_{\Omega_d} r^2\nabla\hat{\gamma}_f\cdot\nabla\varphi+\hat{\gamma}_f\varphi+\left[\sum_{n=1}^{N}\frac{1}{V_n}\int_{P_n}\frac{\partial A}{\partial\gamma_p}\frac{\partial\gamma_p}{\partial\gamma_e}-Re\left(\frac{\partial\epsilon_r^{-1}}{\partial\gamma_p}\frac{\partial\gamma_p}{\partial\gamma_e}\nabla\left(H_{sz}+H_{iz}\right)\right)\cdot Re\left(\nabla\hat{H}_{sz}^*\right)\right.$$
$$\left.+Im\left(\frac{\partial\epsilon_r^{-1}}{\partial\gamma_p}\frac{\partial\gamma_p}{\partial\gamma_e}\nabla\left(H_{sz}+H_{iz}\right)\right)\cdot Im\left(\nabla\hat{H}_{sz}^*\right)\mathrm{d}\Omega\right]\varphi\,\mathrm{d}\Omega=0,\ \forall\varphi\in\mathcal{H}(\Omega_d) \tag{38}$$

where *Re* and *Im* are operators used to extract the real part and imaginary part of a complex.

A.2. Adjoint analysis of topology optimization problem for 3D electromagnetic waves

Based on the Lagrangian multiplier-based adjoint method, the augmented Lagrangian for the topology optimization problem in equation (21) can be written to be

$$\hat{J}=\int_{\Omega}A\left(\mathbf{E}_s^R,\mathbf{E}_s^I,\nabla_{\mathbf{x}}\times\mathbf{E}_s^R,\nabla_{\mathbf{x}}\times\mathbf{E}_s^I,\gamma_p;\gamma\right)+\mu_r^{-1}\left[\nabla\times\left(\mathbf{E}_s^R+\mathbf{E}_i^R\right)\right]\cdot\left(\nabla\times\hat{\mathbf{E}}_s^R\right)$$
$$-k_0^2\left[\epsilon_r^R\left(\mathbf{E}_s^R+\mathbf{E}_i^R\right)-\epsilon_r^I\left(\mathbf{E}_s^I+\mathbf{E}_i^I\right)\right]\cdot\hat{\mathbf{E}}_s^R+\mu_r^{-1}\left[\nabla\times\left(\mathbf{E}_s^I+\mathbf{E}_i^I\right)\right]\cdot\left(\nabla\times\hat{\mathbf{E}}_s^I\right)$$
$$-k_0^2\left[\epsilon_r^I\left(\mathbf{E}_s^R+\mathbf{E}_i^R\right)+\epsilon_r^R\left(\mathbf{E}_s^I+\mathbf{E}_i^I\right)\right]\cdot\hat{\mathbf{E}}_s^I\,\mathrm{d}\Omega+\int_{\Omega_P}\mu_r^{-1}\left(\mathbf{T}\nabla\times\mathbf{E}_s^R\right)\cdot\left(\mathbf{T}\nabla\times\hat{\mathbf{E}}_s^R\right)|\mathbf{T}|^{-1} \tag{39}$$
$$-k_0^2\left(\epsilon_r^R\mathbf{E}_s^R-\epsilon_r^I\mathbf{E}_s^I\right)\cdot\hat{\mathbf{E}}_s^R|\mathbf{T}|+\mu_r^{-1}\left(\mathbf{T}\nabla\times\mathbf{E}_s^I\right)\cdot\left(\mathbf{T}\nabla\times\hat{\mathbf{E}}_s^I\right)|\mathbf{T}|^{-1}$$
$$-k_0^2\left(\epsilon_r^I\mathbf{E}_s^R+\epsilon_r^R\mathbf{E}_s^I\right)\cdot\hat{\mathbf{E}}_s^I|\mathbf{T}|\,\mathrm{d}\Omega+\int_{\Omega_d}r^2\nabla\gamma_f\cdot\nabla\hat{\gamma}_f+\gamma_f\hat{\gamma}_f-\gamma\hat{\gamma}_f\,\mathrm{d}\Omega$$

where $\hat{\mathbf{E}}_s^R\in\mathcal{V}_{\mathbf{E}}$ with $\mathbf{n}\times\hat{\mathbf{E}}_s^R=\mathbf{0}$ on Γ_D, $\hat{\mathbf{E}}_s^I\in\mathcal{V}_{\mathbf{E}}$ with $\mathbf{n}\times\hat{\mathbf{E}}_s^I=\mathbf{0}$ on Γ_D, and $\hat{\gamma}_f\in\mathcal{H}(\Omega_d)$ are the adjoint variables of $\mathbf{E}_s^R\in\mathcal{V}_{\mathbf{E}}$, $\mathbf{E}_s^I\in\mathcal{V}_{\mathbf{E}}$, and $\gamma_f\in\mathcal{H}(\Omega_d)$, respectively; $\mathcal{V}_{\mathbf{E}}$ is defined to be the functional space $\left\{\mathbf{u}\in\mathcal{H}(\mathrm{curl};\Omega\cup\Omega_P)\,\middle|\,\nabla\cdot\mathbf{u}=0\text{ in }\Omega\cup\Omega_P\right\}$ with $\mathcal{H}(\mathrm{curl};\Omega\cup\Omega_P)=\left\{\mathbf{u}\in\left(\mathcal{L}^2(\Omega\cup\Omega_P)\right)^3\,\middle|\,\nabla\times\mathbf{u}\in\left(\mathcal{L}^2(\Omega\cup\Omega_P)\right)^3\right\}$; $\mathcal{L}^2(\Omega\cup\Omega_P)$ represents the second order Lebesque

space for the real functions defined on $\Omega \cup \Omega_P$. The first order variational of the augmented Lagrangian to the field variables and design variable is

$$\begin{aligned}
\delta \hat{J} = & \int_{\Omega} \frac{\partial A}{\partial \mathbf{E}_s^R} \cdot \delta \mathbf{E}_s^R + \frac{\partial A}{\partial \mathbf{E}_s^I} \cdot \delta \mathbf{E}_s^I + \frac{\partial A}{\partial \nabla \times \mathbf{E}_s^R} \cdot \left(\nabla \times \delta \mathbf{E}_s^R \right) + \frac{\partial A}{\partial \nabla \times \mathbf{E}_s^I} \cdot \left(\nabla \times \delta \mathbf{E}_s^I \right) \mathrm{d}\Omega \\
& + \sum_{n=1}^{N} \frac{1}{V_n} \int_{P_n} \frac{\partial A}{\partial \gamma_p} \frac{\partial \gamma_p}{\partial \gamma_e} \delta \gamma_f \, \mathrm{d}\Omega + \int_{\Omega_d} \frac{\partial A}{\partial \gamma} \delta \gamma \, \mathrm{d}\Omega + \int_{\Omega} \mu_r^{-1} \left(\nabla \times \delta \mathbf{E}_s^R \right) \cdot \left(\nabla \times \hat{\mathbf{E}}_s^R \right) \\
& - k_0^2 \left(\epsilon_r^R \delta \mathbf{E}_s^R - \epsilon_r^I \delta \mathbf{E}_s^I \right) \cdot \hat{\mathbf{E}}_s^R \, \mathrm{d}\Omega + \int_{\Omega_P} \mu_r^{-1} \left(\mathbf{T} \nabla \times \delta \mathbf{E}_s^R \right) \cdot \left(\mathbf{T} \nabla \times \hat{\mathbf{E}}_s^R \right) |\mathbf{T}|^{-1} \\
& - k_0^2 \left(\epsilon_r^R \delta \mathbf{E}_s^R - \epsilon_r^I \delta \mathbf{E}_s^I \right) \cdot \hat{\mathbf{E}}_s^R \, |\mathbf{T}| \, \mathrm{d}\Omega + \int_{\Omega} \mu_r^{-1} \left(\nabla \times \delta \mathbf{E}_s^I \right) \cdot \left(\nabla \times \hat{\mathbf{E}}_s^I \right) - k_0^2 \left(\epsilon_r^I \delta \mathbf{E}_s^R + \epsilon_r^R \delta \mathbf{E}_s^I \right) \cdot \hat{\mathbf{E}}_s^I \, \mathrm{d}\Omega \\
& + \int_{\Omega_P} \mu_r^{-1} \left(\mathbf{T} \nabla \times \delta \mathbf{E}_s^I \right) \cdot \left(\mathbf{T} \nabla \times \hat{\mathbf{E}}_s^I \right) |\mathbf{T}|^{-1} - k_0^2 \left(\epsilon_r^I \delta \mathbf{E}_s^R + \epsilon_r^R \delta \mathbf{E}_s^I \right) \cdot \hat{\mathbf{E}}_s^I \, |\mathbf{T}| \, \mathrm{d}\Omega \\
& + \int_{\Omega_d} r^2 \nabla \delta \gamma_f \cdot \nabla \hat{\gamma}_f + \delta \gamma_f \hat{\gamma}_f - \delta \gamma \hat{\gamma}_f \, \mathrm{d}\Omega - \sum_{n=1}^{N} \frac{1}{V_n} \int_{P_n} k_0^2 \left[\frac{\partial \epsilon_r^R}{\partial \gamma_p} \left(\mathbf{E}_s^R + \mathbf{E}_i^R \right) - \frac{\partial \epsilon_r^I}{\partial \gamma_p} \left(\mathbf{E}_s^I + \mathbf{E}_i^I \right) \right] \cdot \hat{\mathbf{E}}_s^R \frac{\partial \gamma_p}{\partial \gamma_e} \delta \gamma_f \\
& + k_0^2 \left[\frac{\partial \epsilon_r^I}{\partial \gamma_p} \left(\mathbf{E}_s^R + \mathbf{E}_i^R \right) + \frac{\partial \epsilon_r^R}{\partial \gamma_p} \left(\mathbf{E}_s^I + \mathbf{E}_i^I \right) \right] \cdot \hat{\mathbf{E}}_s^I \frac{\partial \gamma_p}{\partial \gamma_e} \delta \gamma_f \, \mathrm{d}\Omega
\end{aligned} \tag{40}$$

where $\delta \mathbf{E}_s^R$, $\delta \mathbf{E}_s^I$, $\delta \gamma_f$ and $\delta \gamma$ are the first order variational of $\mathbf{E}_s^R$, $\mathbf{E}_s^I$, γ_f and γ, respectively. From the Kurash–Kuhn–Tucker condition of the partial differential equation constrained optimization problem [54], the first order variational of the augmented Lagrangian to the field variables satisfies

$$\begin{aligned}
& \int_{\Omega} \frac{\partial A}{\partial \mathbf{E}_s^R} \cdot \delta \mathbf{E}_s^R + \frac{\partial A}{\partial \nabla \times \mathbf{E}_s^R} \cdot \left(\nabla \times \delta \mathbf{E}_s^R \right) + \mu_r^{-1} \left(\nabla \times \delta \mathbf{E}_s^R \right) \cdot \left(\nabla \times \hat{\mathbf{E}}_s^R \right) - k_0^2 \delta \mathbf{E}_s^R \cdot \left(\epsilon_r^R \hat{\mathbf{E}}_s^R + \epsilon_r^I \hat{\mathbf{E}}_s^I \right) \mathrm{d}\Omega \\
& + \int_{\Omega_P} \mu_r^{-1} \left(\mathbf{T} \nabla \times \delta \mathbf{E}_s^R \right) \cdot \left(\mathbf{T} \nabla \times \hat{\mathbf{E}}_s^R \right) |\mathbf{T}|^{-1} - k_0^2 \delta \mathbf{E}_s^R \cdot \left(\epsilon_r^R \hat{\mathbf{E}}_s^R + \epsilon_r^I \hat{\mathbf{E}}_s^I \right) |\mathbf{T}| \, \mathrm{d}\Omega = 0
\end{aligned} \tag{41}$$

$$\begin{aligned}
& \int_{\Omega} \frac{\partial A}{\partial \mathbf{E}_s^I} \cdot \delta \mathbf{E}_s^I + \frac{\partial A}{\partial \nabla \times \mathbf{E}_s^I} \cdot \left(\nabla \times \delta \mathbf{E}_s^I \right) + \mu_r^{-1} \left(\nabla \times \delta \mathbf{E}_s^I \right) \cdot \left(\nabla \times \hat{\mathbf{E}}_s^I \right) - k_0^2 \delta \mathbf{E}_s^I \cdot \left(\epsilon_r^R \hat{\mathbf{E}}_s^I - \epsilon_r^I \hat{\mathbf{E}}_s^R \right) \mathrm{d}\Omega \\
& + \int_{\Omega_P} \mu_r^{-1} \left(\mathbf{T} \nabla \times \delta \mathbf{E}_s^I \right) \cdot \left(\mathbf{T} \nabla \times \hat{\mathbf{E}}_s^I \right) |\mathbf{T}|^{-1} - k_0^2 \delta \mathbf{E}_s^I \cdot \left(\epsilon_r^R \hat{\mathbf{E}}_s^I - \epsilon_r^I \hat{\mathbf{E}}_s^R \right) |\mathbf{T}| \, \mathrm{d}\Omega = 0
\end{aligned} \tag{42}$$

$$\begin{aligned}
& \int_{\Omega_d} r^2 \nabla \delta \gamma_f \cdot \nabla \hat{\gamma}_f + \delta \gamma_f \hat{\gamma}_f \, \mathrm{d}\Omega + \sum_{n=1}^{N} \frac{1}{V_n} \int_{P_n} \frac{\partial A}{\partial \gamma_p} \frac{\partial \gamma_p}{\partial \gamma_e} \delta \gamma_f - k_0^2 \left[\frac{\partial \epsilon_r^R}{\partial \gamma_p} \left(\mathbf{E}_s^R + \mathbf{E}_i^R \right) - \frac{\partial \epsilon_r^I}{\partial \gamma_p} \left(\mathbf{E}_s^I + \mathbf{E}_i^I \right) \right] \\
& \cdot \hat{\mathbf{E}}_s^R \frac{\partial \gamma_p}{\partial \gamma_e} \delta \gamma_f - k_0^2 \left[\frac{\partial \epsilon_r^I}{\partial \gamma_p} \left(\mathbf{E}_s^R + \mathbf{E}_i^R \right) + \frac{\partial \epsilon_r^R}{\partial \gamma_p} \left(\mathbf{E}_s^I + \mathbf{E}_i^I \right) \right] \cdot \hat{\mathbf{E}}_s^I \frac{\partial \gamma_p}{\partial \gamma_e} \delta \gamma_f \, \mathrm{d}\Omega = 0
\end{aligned} \tag{43}$$

And the adjoint sensitivity can be derived to be the first order variational of the augmented Lagrangian to the design variable

$$\delta \hat{J} = \int_{\Omega_d} \left(\frac{\partial A}{\partial \gamma} - \hat{\gamma}_f \right) \delta \gamma \, \mathrm{d}\Omega \tag{44}$$

Without losing the arbitrariness of $\delta \mathbf{E}_s^R$, $\delta \mathbf{E}_s^I$ and $\delta \gamma_f$, one can set $\delta \mathbf{E}_s^R = \delta \mathbf{E}_s^I = \boldsymbol{\phi}$ with $\forall \boldsymbol{\phi} \in \mathcal{V}_{\mathbf{E}}$ and $\delta \gamma_f = \varphi$ with $\forall \varphi \in \mathcal{H}(\Omega_d)$. By substituting $\boldsymbol{\phi}$ and φ into equations (41), (42) and (43), and adding equation (42) multiplied by $-j$ to equation (41), the adjoint equations for the topology optimization problem in equation (15) can be derived to be: find $\hat{\mathbf{E}}_s$ with $Re\left(\hat{\mathbf{E}}_s\right) \in \mathcal{V}_{\mathbf{E}}$, $Im\left(\hat{\mathbf{E}}_s\right) \in \mathcal{V}_{\mathbf{E}}$ and $\mathbf{n} \times \hat{\mathbf{E}}_s = \mathbf{0}$ on Γ_D, satisfying

$$\int_{\Omega}\left(\frac{\partial A}{\partial Re\left(\mathbf{E}_s\right)}-j\frac{\partial A}{\partial Im\left(\mathbf{E}_s\right)}\right)\cdot\boldsymbol{\phi}+\left(\frac{\partial A}{\partial\nabla\times Re\left(\mathbf{E}_s\right)}-j\frac{\partial A}{\partial\nabla\times Im\left(\mathbf{E}_s\right)}\right)\cdot\left(\nabla\times\boldsymbol{\phi}\right)$$
$$+\mu_r^{-1}\left(\nabla\times\hat{\mathbf{E}}_s^*\right)\cdot\left(\nabla\times\boldsymbol{\phi}\right)-k_0^2\epsilon_r\hat{\mathbf{E}}_s^*\cdot\boldsymbol{\phi}\,\mathrm{d}\Omega+\int_{\Omega_P}\mu_r^{-1}\left(\mathbf{T}\nabla\times\hat{\mathbf{E}}_s^*\right)\cdot\left(\mathbf{T}\nabla\times\boldsymbol{\phi}\right)|\mathbf{T}|^{-1} \tag{45}$$
$$-k_0^2\epsilon_r\hat{\mathbf{E}}_s^*\cdot\boldsymbol{\phi}\,|\mathbf{T}|\,\mathrm{d}\Omega=0,\forall\boldsymbol{\phi}\in\mathcal{V}_{\mathbf{E}}$$

find $\hat{\gamma}_f\in\mathcal{H}\left(\Omega_d\right)$ satisfying

$$\int_{\Omega_d}r^2\nabla\hat{\gamma}_f\cdot\nabla\varphi+\hat{\gamma}_f\varphi+\left[\sum_{n=1}^{N}\frac{1}{V_n}\int_{P_n}\frac{\partial A}{\partial\gamma_p}\frac{\partial\gamma_p}{\partial\gamma_e}-Re\left(k_0^2\frac{\partial\epsilon_r}{\partial\gamma_p}\frac{\partial\gamma_p}{\partial\gamma_e}\left(\hat{\mathbf{E}}_s+\hat{\mathbf{E}}_i\right)\right)\cdot Re\left(\hat{\mathbf{E}}_s^*\right)\right.$$
$$\left.+Im\left(k_0^2\frac{\partial\epsilon_r}{\partial\gamma_p}\frac{\partial\gamma_p}{\partial\gamma_e}\left(\hat{\mathbf{E}}_s+\hat{\mathbf{E}}_i\right)\right)\cdot Im\left(\hat{\mathbf{E}}_s^*\right)\mathrm{d}\Omega\right]\varphi\,\mathrm{d}\Omega=0,\ \forall\varphi\in\mathcal{H}\left(\Omega_d\right) \tag{46}$$

References

[1] A.Y. Piggott, J. Lu, K.G. Lagoudakis, J. Petykiewicz, T.M. Babinec, J. Vučović, Inverse design and demonstration of a compact and broadband on-chip wavelength demultiplexer, Nat. Photonics 9 (2015) 374–377.
[2] B. Shen, P. Wang, R. Polson, R. Menon, An integrated-nanophotonics polarization beamsplitter with 2.4 × 2.4 μm^2 footprint, Nat. Photonics 9 (2015) 378–382.
[3] L.H. Frandsen, Y. Elesin, L.F. Frellsen, M. Mitrovic, Y. Ding, O. Sigmund, K. Yvind, Topology optimized mode conversion in a photonic crystal waveguide fabricated in silicon-on-insulator material, Opt. Express 22 (2014) 8525–8532.
[4] O. Sigmund, K.G. Hougaard, Geometric properties of optimal photonic crystals, Phys. Rev. Lett. 100 (2008) 153904.
[5] J. Andkjær, O. Sigmund, Topology optimized low-contrast all-dielectric optical cloak, Appl. Phys. Lett. 98 (2011) 021112.
[6] J. Andkjær, N.A. Mortensen, O. Sigmund, Towards all-dielectric, polarization-independent optical cloaks, Appl. Phys. Lett. 100 (2012) 101106.
[7] G. Fujii, H. Watanabe, T. Yamada, T. Ueta, M. Mizuno, Level set based topology optimization for optical cloaks, Appl. Phys. Lett. 102 (2013) 251106.
[8] A.R. Diaz, O. Sigmund, A topology optimization method for design of negative permeability metamaterials, Struct. Multidiscip. Optim. 41 (2010) 163–177.
[9] S. Zhou, W. Li, G. Sun, Q. Li, A level-set procedure for the design of electromagnetic metamaterials, Opt. Express 18 (2010) 6693–6702.
[10] S. Zhou, W. Li, Y. Chen, G. Sun, Q. Li, Topology optimization for negative permeability metamaterials using level-set algorithm, Acta Mater. 59 (2011) 2624–2636.
[11] J. Andkjær, S. Nishiwaki, T. Nomura, O. Sigmund, Topology optimization of grating couplers for the efficient excitation of surface plasmons, J. Opt. Soc. Am. B, Opt. Phys. 27 (2010) 1828–1832.
[12] S. Zhou, W. Li, Q. Li, Level-set based topology optimization for electromagnetic dipole antenna design, J. Comput. Phys. 229 (2010) 6915–6930.
[13] E. Hassan, E. Wadbro, M. Berggren, Topology optimization of metallic antennas, IEEE Trans. Antennas Propag. 62 (2014) 2488–2500.
[14] Y. Deng, Z. Liu, C. Song, J. Wu, Y. Liu, Y. Wu, Topology optimization-based computational design methodology for surface plasmon polaritons, Plasmonics 10 (2015) 569–583.
[15] Y. Deng, J.G. Korvink, Topology optimization for three-dimensional electromagnetic waves using an edge element-based finite-element method, Proc. R. Soc. A 472 (2016) 20150835.
[16] H. Shim, V.T.T. Ho, S. Wang, D.A. Tortorelli, Level set-based topology optimization for electromagnetic systems, IEEE Trans. Magn. 45 (2009) 1582–1585.
[17] T. Feichtner, O. Selig, M. Kiunke, B. Hecht, Evolutionary optimization of optical antennas, Phys. Rev. Lett. 109 (2012) 127701.
[18] T. Nomura, K. Sato, K. Taguchi, T. Kashiwa, S. Nishiwaki, Structural topology optimization for the design of broadband dielectric resonator antennas using the finite difference time domain technique, Int. J. Numer. Methods Eng. 71 (2007) 1261–1296.
[19] M.B. Duhring, J.S. Jensen, O. Sigmund, Acoustic design by topology optimization, J. Sound Vib. 317 (2008) 557–575.
[20] A. Erentok, O. Sigmund, Topology optimization of sub-wavelength antennas, IEEE Trans. Antennas Propag. 59 (2011) 58–69.
[21] M. Otomori, T. Yamada, K. Izui, S. Nishiwaki, J. Andkjær, A topology optimization method based on the level set method for the design of negative permeability dielectric metamaterials, Comput. Methods Appl. Mech. Eng. 237–240 (2012) 192–211.
[22] A.G.M. Michell, The limit of economy of material in frame-structures, Philos. Mag. 8 (1904) 589–597.
[23] M. Bendsøe, N. Kikuchi, Generating optimal topologies in optimal design using a homogenization method, Comput. Methods Appl. Mech. Eng. 71 (1988) 197–224.
[24] G.I.N. Rozvany, Aims scope methods history and unified terminology of computer-aided optimization in structural mechanics, Struct. Multidiscip. Optim. 21 (2001) 90–108.
[25] A. Gersborg-Hansen, M.P. Bendsøe, O. Sigmund, Topology optimization of heat conduction problems using the finite volume method, Struct. Multidiscip. Optim. 31 (2006) 251–259.
[26] W. Akl, A. El-Sabbagh, K. Al-Mitani, A. Baz, Topology optimization of a plate coupled with acoustic cavity, Int. J. Solids Struct. 46 (2008) 2060–2074.
[27] S. Kreissl, G. Pingen, K. Maute, An explicit level-set approach for generalized shape optimization of fluids with the lattice Boltzmann method, Int. J. Numer. Methods Fluids 65 (2011) 496–519.
[28] S. Zhou, Q. Li, A variational level set method for the topology optimization of steady-state Navier–Stokes flow, J. Comput. Phys. 227 (2008) 10178–10195.
[29] J.K. Guest, J.H. Prevost, Topology optimization of creeping fluid flows using a Darcy–Stokes finite element, Int. J. Numer. Methods Eng. 66 (2006) 461–484.
[30] T. Borrvall, J. Petersson, Topology optimization of fluid in Stokes flow, Int. J. Numer. Methods Fluids 41 (2003) 77–107.
[31] M. Bendsøe, O. Sigmund, Topology Optimization—Theory, Methods and Applications, Springer, Berlin, 2003.
[32] Y. Deng, Y. Wu, Z. Liu, Topology Optimization Theory for Laminar Flow, Springer, Singapore, 2018.
[33] A. Takezawa, M. Haraguchi, T. Okamoto, M. Kitamura, Cross-sectional optimization of whispering-gallery mode sensor with high electric field intensity in the detection domain, IEEE J. Sel. Top. Quantum Electron. 20 (6) (2014) 1–10.
[34] A. Takezawa, M. Kitamura, Cross-sectional shape optimization of whispering-gallery ring resonators, IEE/OSA J. Lightwave Technol. 30 (2012) 2776–2782.

[35] Y. Elesin, B.S. Lazarov, J.S. Jensen, O. Sigmund, Time domain topology optimization of 3D nanophotonic devices, Photonics Nanostruct. Fundam. Appl. 12 (2014) 23–33.
[36] X. Zhao, S. Huang, H. Du, Theoretical analysis and numerical experiments of variational adjoint approach for refractivity estimation, Radio Sci. 46 (2011) RS1006.
[37] J.S. Jensen, O. Sigmund, Topology optimization of photonic crystal structures: a high-bandwidth low-loss T-junction waveguide, J. Opt. Soc. Am. B 22 (2005) 1191–1198.
[38] F.M. Mahomed, R. Naz, A note on the Lie symmetries of complex partial differential equations and their split real systems, Pramana 77 (2011) 483–491.
[39] S. Ali, F.M. Mahomed, A. Qadir, Complex Lie symmetries for variational problems, J. Nonlinear Math. Phys. 15 (2008) 25–35.
[40] J. Jin, The Finite Element Method in Electromagnetics, 2nd edition, John Wiley & Sons, New York, 2002.
[41] D. Sarid, W.A. Challener, Modern Introduction to Surface Plasmons: Theory, Mathematica Modeling, and Applications, 1st edition, Cambridge University Press, 2010.
[42] J. Berenger, A perfectly matched layer for the absorption of electromagnetic waves, J. Comput. Phys. 114 (1994) 185–200.
[43] W. Shin, S. Fan, Choice of the perfectly matched layer boundary condition for frequency-domain Maxwell's equations solvers, J. Comput. Phys. 231 (2012) 3406–3431.
[44] O. Sigmund, Morphology-based black and white filters for topology optimization, Struct. Multidiscip. Optim. 33 (2007) 401–424.
[45] B. Lazarov, O. Sigmund, Filters in topology optimization based on Helmholtz type differential equations, Int. J. Numer. Methods Eng. 86 (2011) 765–781.
[46] K. Svanberg, The method of moving asymptotes: a new method for structural optimization, Int. J. Numer. Methods Eng. 24 (1987) 359–373.
[47] J.C. Nedelec, Mixed finite elements in R^3, Numer. Math. 35 (1980) 315–341.
[48] J.C. Nedelec, A new family of mixed finite elements in R^3, Numer. Math. 50 (1986) 57–81.
[49] Y. Deng, Z. Liu, P. Zhang, Y. Liu, Y. Wu, Topology optimization of unsteady incompressible Navier–Stokes flows, J. Comput. Phys. 230 (2011) 6688–6708.
[50] L.B. Olesen, F. Okkels, H. Bruus, A high-level programming language implementation of topology optimization applied to flow, steady-state Navier–Stokes, Int. J. Numer. Methods Eng. 65 (2006) 975–1001.
[51] J. Guest, J. Prevost, T. Belytschko, Achieving minimum length scale in topology optimization using nodal design variables and projection functions, Int. J. Numer. Methods Eng. 61 (2004) 238–254.
[52] F. Wang, B.S. Lazarov, O. Sigmund, On projection methods, convergence and robust formulations in topology optimization, Struct. Multidiscip. Optim. 43 (2011) 767–784.
[53] Y. Deng, Z. Liu, C. Song, P. Hao, Y. Wu, Y. Liu, J.G. Korvink, Topology optimization of metal nanostructures for localized surface plasmon resonances, Struct. Multidiscip. Optim. 53 (2016) 967–972.
[54] M. Hinze, R. Pinnau, M. Ulbrich, S. Ulbrich, Optimization with PDE Constraints, Springer, Berlin, 2009.
[55] P. Monk, Finite Element Methods for Maxwell's Equations, Oxford University Press, 2003.
[56] K.H. Su, Q.H. Wei, X. Zhang, J.J. Mock, D.R. Smith, S. Schultz, Interparticle coupling effects on plasmon resonances of nanogold particles, Nano Lett. 3 (2003) 1087–1090.
[57] M. Moskovits, Surface-enhanced spectroscopy, Rev. Mod. Phys. 57 (1985) 783.
[58] K.M. McPeak, S.V. Jayanti, S.J.P. Kress, S. Meyer, S. Iotti, A. Rossinelli, D.J. Norris, Plasmonic films can easily be better: rules and recipes, ACS Photonics 2 (2015) 326–333.